Department of Precision and Microsystems Engineering

Finite Element Simulation of Light and Correlation Propagation in Tissue

Wenpei Guo

Report no : 2023.065
Coach : Binbin Zhang
Professor : Nandini Bhattacharya
Specialisation : Optics
Type of report : Master Thesis
Date : 16-08-2023

Finite Element Simulation of Light and Correlation Propagation in Tissue

A finite element model simulation of diffuse optics in static and dynamic conditions

by

Wenpei Guo

to obtain the degree of Master of Science
at the Delft University of Technology,
to be defended publicly on Thursday August 24, 2023 at 10:00 AM.

Student number:	5594952	
Project duration:	September 1, 2022 – Angust 10, 2023	
Thesis committee:	Dr. N. (Nandini) Bhattacharya,	TU Delft, supervisor
	Dr. Sophinese Iskander-Rizk,	TU Delft
	B.Zhang,	Acme Corporation

This thesis is confidential and cannot be made public until December 31, 2024.

Cover:	Canadarm 2 Robotic Arm Grapples SpaceX Dragon by NASA under CC BY-NC 2.0 (Modified)
Style:	TU Delft Report Style, with modifications by Daan Zwaneveld

An electronic version of this thesis is available at `http://repository.tudelft.nl/`.

TU Delft

Abstract

The investigation of the interaction between lasers and brain tissue holds significant theoretical and practical significance in the field of brain physiology studies. A two-dimensional finite element-based simulation model was constructed using the commercial finite element simulation software COMSOL Multiphysics to investigate the propagation of light and photon correlation in tissues. The simulations included static and dynamic conditions of light propagation in tissue. In both cases this diffuse light propagation itself was studied along with photon correlation using the solution of the diffusion equation. Subsequently, the obtained simulation results are assessed and summarized by considering the outcomes of data fitting. The findings indicate that the accuracy of simulating light propagation is higher for larger sizes, although satisfactory results can be achieved for correlation propagation simulations in the small size range. The simulation results remain unaffected by the refinement of the mesh, provided that the fundamental criteria for mesh size are satisfied.

Contents

1

Introduction

1.1. Introduction

The process of blood circulation within the human body is primarily responsible for transporting oxygen and eliminating metabolic waste products. Dysregulated blood circulation can give rise to various complications, encompassing tissue ulcers, paralysis, and even mortality, contingent upon the specific region impacted. Abnormal blood flow conditions can also serve as a basis for diagnosing various disorders. Nevertheless, conventional intrusive diagnostic techniques may induce further discomfort among patients. The growing prevalence of non-invasive and minimally invasive medical testing in contemporary medicine has been propelled by notable advancements. Consequently, this has fostered the emergence and refinement of medical imaging technologies. The field of diffuse optics, which is seeing significant growth, presents a promising avenue to address these requirements.

The present research commences by providing a comprehensive summary of recent advancements in diffuse optics. In recent years, there has been significant progress in developing near-infrared spectroscopy (NIRS) and diffuse correlation spectroscopy (DCS) techniques for non-invasive blood flow measurement. NIRS can consistently assess the reduction in light intensity as it traverses the cerebral cortex without causing any harm or intrusion. This methodology is employed to quantify the optical characteristics of the medium, encompassing absorption, and scattering. Blood flow can be evaluated by inferring physical qualities based on the aforementioned visual features. It is important to acknowledge that Near-Infrared Spectroscopy (NIRS) does not consider coherent characteristics.

Diffuse correlation spectroscopy (DCS) is a technique that offers a direct and robust optical assessment of microvascular blood flow. It leverages the coherence of light to quantify the dynamic characteristics of a medium, namely the blood flow within tissue. Various clinical disorders, such as cardiovascular disease, stroke, head trauma, peripheral artery disease, and cancer, are linked to abnormal blood flow. Hence, the utilization of DCS holds significant potential in offering valuable insights for diagnosing diseases mentioned above and evaluating the effectiveness of therapy interventions.

It is noteworthy to emphasize that biological tissues are characterized by a higher degree of complexity. The human body consists of static components, such as bones and muscles, and dynamic components, such as blood and tissue fluids. Therefore, it is important to develop a reliable model that can effectively replicate the coexistence of these two aspects. This is an area of research that warrants further exploration. Before establishing a connection between the two variables, it is important to analyse and synthesize their respective simulations in isolation.

Suitable simulation approaches can be employed to investigate the interaction between light and tissue in intricate tissue geometries. In modeling the interaction between light and biological tissue, the initial phase often involves the computation of the light distribution within the tissue, considering the optical characteristics of the illuminating source. The inverse model enables the deduction of information about the medium based on light measurements.

The subsequent section of the report delineates methodologies employed in modeling the intricate interplay between light and biological tissue. The Radiative Transfer Equation (RTE) is a mathematical framework for elucidating how light propagates through a tissue. One can ascertain the light distribution within that tissue by solving the RTE. The diffusion equation can approximate the RTE under specific circumstances. These conditions include a much higher reduced scattering coefficient than the absorption coefficient and a research site that is distant from the source or boundary. The optical density diffusion problem can be effectively solved using the finite element technique (FEM). The Finite Element Method (FEM) simplifies the radiative transfer equation by assuming isotropic light transport. One notable benefit of this approach is its computing efficiency, enabling swift data processing. Moreover, it yields precise outcomes even in places far from the primary light source. Nevertheless, implementing the Finite Element Method (FEM) exhibits intricacy, and its precision is constrained when dealing with regions close to the light source.

An alternative methodology that might be employed is utilizing Monte Carlo simulation. Monte Carlo (MC) simulation for light propagation in tissue is the gold standard. Since this report does not contain MC simulations, only a brief description is given.

A model is developed to represent the diffusion approximation of the Radiative Transfer Equation (RTE) and the Correlation Transfer Equation (CTE). This study examines a simplified simulation of the RTE and the CTE by applying the Finite Element Method. A numerical simulation model of a single-layer diffusion tissue is constructed using the commercially available finite element simulation software COMSOL Multiphysics. The MATLAB software is utilized to analyze the data and assess the accuracy of the simulation. The analysis and summarization of the simulation accuracy are conducted considering the impact of the model parameter values. The transmission under consideration can be characterized by either the diffusion equation or the Helmholtz equation.

The Chapter 2 of this paper commences with an introductory overview of the fundamental principles behind diffuse optics and the simulation of light propagation. The findings of the simulations of the Radiative Transport Equation (RTE) and the Correlation Transport Equation (CTE) are presented in Chapters 3 and 4, respectively. Chapter 5 of the study integrates and contrasts the two aforementioned entities, while also conducting an analysis of the divergences in particular arrangements between the two, despite the use of similar methodologies. The Chapter 6 concludes.

2

Background

2.1. Near-Infrared Spectroscopy

As the name implies, Near-Infrared Spectroscopy(NIRS) uses near-infrared light to detect the absorption and scattering properties of media. NIRS mainly concentrates on optical properties. It is an emerging non-invasive monitoring modality based on the absorption of infrared light-emitting chromophores [12]. In 1977[20], Jobsis and his team applied NIRS spectroscopy to measure cerebral hemodynamics in humans, confirming that NIRS spectroscopy could be applied to probe the optical properties of thicker tissues. Previously, NIRS had only been used to detect blood flow in shallow tissues.

In contrast to other methodologies, Near-Infrared Spectroscopy (NIRS) measures diffuse light, which is scattered many times, and then individual photon trajectories are random walks. So they are estimated by a diffusion equation. Consequently, this methodology is frequently denoted as diffuse spectroscopy (DOS). The main idea behind NIRS is to illuminate the tissue with light, measure the light before and after it passes through the tissue, and then use a suitable model to explain the difference between the incident light and the detected light.NIRS is generally divided into three categories depending on the type of incident light and what the detector is measuring, which are Continuous Wave (CW-NIRS), Frequency Domain (FD-NIRS), and Time Domain (TD-NIRS).

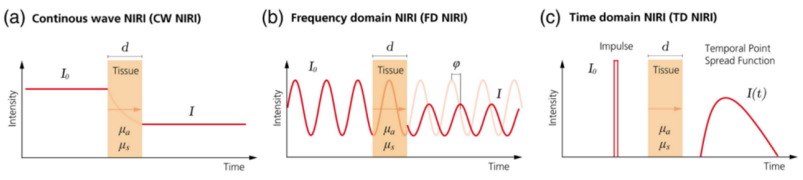

Figure 2.1: Comparison of the three variants of NIRS[34]

The comparison of these three types of NIRS is shown in figure2.1. The CW systems use constant-amplitude continuous light and use light attenuation to measure absorption. The main limitation of CW-NIRS is that the measured drop in intensity may be from scattering and absorption, but we cannot

separate these two effects.FD-NIRS systems use amplitude-modulated continuous light and measure the attenuation and phase shift, or phase delay, to get information about absorption and scattering properties.

TD-NIRS systems use extremely short pulses of light, which are on the order of a few picoseconds, and measure the time-of-flight of individual photons to determine absorption, scattering, and the path length of the photon to provide depth resolution. And the detected intensity profile is called Time Point Spread Function (TPSF)□ which will be described in detail in the following sections.

2.1.1. Basic Optics Theory

Before we start a more detailed discussion of near-infrared spectroscopy, we first review some of the basic concepts and formulas of light involved in NIRS technology to better understand NIRS technology.

It is well known that light is an electromagnetic wave that is both fluctuating and particle-based, the simplest being a monochromatic plane simple harmonic. Here we ignore the effects of spatial extent and polarisation, and a one-dimensional scalar description of a light wave can be written that[16],

$$E(x,t) = E_0 cos(kx - \omega t + \phi) = Re\{E_0 e^{i(kx-\omega t+\phi)}\} \tag{2.1}$$

In practice, optical instruments measure the light intensity I,

$$I(x) = \frac{\langle |E(x,t)|^2 \rangle}{\eta} = \frac{\langle |\tilde{E}(x,t)|^2 \rangle}{2\eta} = \frac{\langle \tilde{E}(x,t)\tilde{E}^*(x,t) \rangle}{2\eta} = \frac{E_0^2}{2\eta} \tag{2.2}$$

Where the quantity $\eta = (\mu/\epsilon)fv$, is known as the impedance of free space, and the E^* is the complex conjugate.
The sharp brackets denote the time average,

$$\langle f \rangle = \lim_{T\to\infty} \frac{1}{T} \int_0^T f(t)dt \tag{2.3}$$

Since the NIRS technique is based on the absorption and scattering of light, the absorption and scattering coefficients of the medium are measured to obtain the optical properties of the medium. So before that, it is necessary to introduce the absorption and scattering of light.

Absorption

When light impinges onto matter, it will either be scattered or absorbed. When the energy of the photon matches the energy level difference of the atom, the photon is absorbed and energy is released as heat. This phenomenon can be qualified by using Beer–Lambert law, which is the fundamental law of light absorption,

$$I(\lambda) = I_0(\lambda) e^{-\mu_a(\lambda)\rho} \tag{2.4}$$

Lambert's law states that when light intensity propagates through a medium, the loss of light intensity is proportional to the intensity and path length. Beer's law states that the transmittance of a solution remains constant if the product of the concentration and the length of the light path remains constant[1]. A modern derivation of the Beer-Lambert law combines these two laws and relates absorbance to the

concentration of the attenuating substance and the thickness of the material sample.

The canonical form is,

$$A(\lambda) \equiv -log\frac{I(\lambda)}{I_0(\lambda)} = \mu_a(\lambda)\rho \tag{2.5}$$

$A(\lambda)$ denotes attenuation, or optical density, and defines $-log\frac{I}{I_0}$ as the attenuation. Where I is the light intensity measured by the detector and I_0 is the incident light intensity emitted by the light source. ρ is the source-detector separation and $\mu_a(\lambda)$ is the absorption coefficient.
This law also states that in a solution,$\mu_a(\lambda)$ is proportional to the concentrations of chromophores(light-absorbing compounds).

$$\mu_a(\lambda) = \sum_i c_i\epsilon_i(\lambda) \tag{2.6}$$

where c_i is the concentration of a chromophore and ϵ_i is the proportional term which is also called extinction. Therefore, the attenuation of light in a medium is proportional to the concentration of the absorbing medium and the concentration of light propagating through the medium. In addition, the extinction coefficient is a characteristic that determines the extent to which a species absorbs or reflects radiation or light at a particular wavelength[22], it is wavelength-dependent so it can be simply written as a function of the wavelength λ. This equation holds when the concentration is uniform along the optical path, the chromophores are independent of each other and scattering is not taken into account.

Scattering

Scattering is divided into elastic scattering and inelastic scattering. Particles that undergo elastic scattering continue to have the same energy and wavelength, the main types being Rayleigh scattering and Mie scattering. In inelastic scattering, there is energy transfer, and the wavelength of the photon is not maintained, a typical example is Raman scattering.

Rayleigh's law of scattering applies to tiny particles whose size is much smaller than the wavelength of light. It is scattering where the frequency and wavelength of the scattered light are the same as the incident light and its intensity is inversely proportional to the wavelength λ^4 of the incident light. Rayleigh's law of scattering can be used to explain the blue colour of the sky and the yellow colour of the sun[14].

When the size of the particle radius is close to or greater than the wavelength λ of the incident light, most of the incident light will be scattered along the forward direction, and this phenomenon is called Mie scattering. The degree of Mie scattering is independent of the wavelength, and the properties of the photon after scattering will not change.

A small proportion of the scattered photons, about one in ten million, collide inelastically with the molecules of the medium, resulting in an exchange of energy and a change in wavelength, frequency, and energy after scattering, known as Raman scattering[18].

Light is absorbed and scattered in human tissue. In human tissue, static scattering is mainly from the skin, connective, and cellular organelles. Dynamic scattering is mainly due to the movement of

red blood cells. The scattering coefficient μ_s describes the scattering properties of a material and is defined as the inverse of the average distance a photon travels before it is scattered. Usually, we use a simplified scattering coefficient $\mu'_s \equiv \mu_s(1-g)$ which is called reduced scattering coefficient, where g is the anisotropy factor $g \equiv \langle cos\theta \rangle$ as the average of the cosine of the scattering angle.

2.1.2. Continuous Wave(CW-NIRS)

Continuous-wave near-infrared spectroscopy (CW-NIRS) operates through the emission of a continuous beam of near-infrared light onto the specific tissue of interest, assessing the intensity of the reflected or transmitted light. CW-NIRS allows for the non-invasive measurement of physiological parameters such as tissue oxygenation levels, blood volume, and concentration of specific biomolecules by measuring variations in light intensity. The principles of light absorption and scattering in the near-infrared band of the electromagnetic spectrum are used in this technology to provide valuable insights into the underlying biological processes. However, the CW system measures light attenuation simply by measuring the intensity of the incident light and the intensity of the detected light. This reduction in intensity can come from either scattering or absorption, and it is only possible to distinguish between these two factors by making assumptions.

If human tissue does not scatter light, then the absorption coefficient can be calculated by the Beer-Lambert Law. In reality, however, the scattering coefficient is far greater than the absorption coefficient by several orders of magnitude, violating the premise of the Beer-Lambert Law that the medium is non-scattering. So Deply et al. proposed a modified Beer-Lambert Law, which is as follows[11],

$$A \equiv -log\frac{I}{I_0} = \mu_a \langle \rho \rangle + G \tag{2.7}$$

Where the $\langle \rho \rangle = B\rho$ is the mean optical wavelength, and B is the differential pathlength factor(DPF) that explains the increased travel distance due to scattering. DPF depends on the scattering and absorption coefficient and is measured experimentally. And G accounts for losses due to scattering and the measurement geometry.

The simplicity, portability, and real-time monitoring capabilities of CW-NIRS make it a versatile and widely utilized tool in diverse research domains, including neuroscience, sports science, clinical diagnostics, and monitoring of cerebral hemodynamics.

The main limitation of CW-NIRS is that the measured decrease in intensity can come from both scattering and absorption. If no assumptions are made about the medium, it is not possible to separate these two effects based on the measurements. Frequency Domain(FD-NIRS) can solve this problem to some extent.

2.1.3. Frequency Domain(FD-NIRS)

The FD-NIRS system uses amplitude-modulated continuous light and measures attenuation and phase shift. This measurement method measures the intensity change and phase delay of the light as it

passes through the tissue. Compared to CW-NIRS, the added phase shift results help to distinguish between attenuation due to absorption and scattering effects.

2.1.4. Time Domain(TD-NIRS)

The TD-NIRS system uses a light source with very short pulses of light, which is on the order of a few picoseconds, and measures the time-of-flight(TOF) of the individual photon to determine the absorption, scattering, and path length of the photons to provide depth resolution. When the pulse leaves the tissue, it is delayed, attenuated, and broadened. As the input short laser pulse is very short, it can be considered as a ”point” in time, and how it propagates over time is also measured. The intensity distribution detected by the short laser pulses passing through the tissue in TD-NIRS is the time point spread function (TPSF). TPSF can be considered to be the impulse response of the medium. Sometimes the FD-NIRS and TD-NIRS are together called time-resolved spectroscopy (TRS).

In TD-NIRS, photons will spread through the tissue due to the absorption and scattering features of the brief laser pulses. Some photons will pass through the tissue and directly reach the detector from the light source, while others will penetrate deep into the tissue, and some will never get to the detector due to absorption effects. In general, it is commonly believed that photons that arrive at the detector late travel a more extended trip and penetrate deeper into the tissue. As a result, for multi-layered media, such as the human head depicted in figure2.2, we can choose the range of photon arrival times to be measured by time-gating and only measure the change in intensity of just the late photons arriving in the time range of interest. This enables the measurement of changes in optical characteristics in deeper layers, which reduces the impact of undesired contributions on the measure.

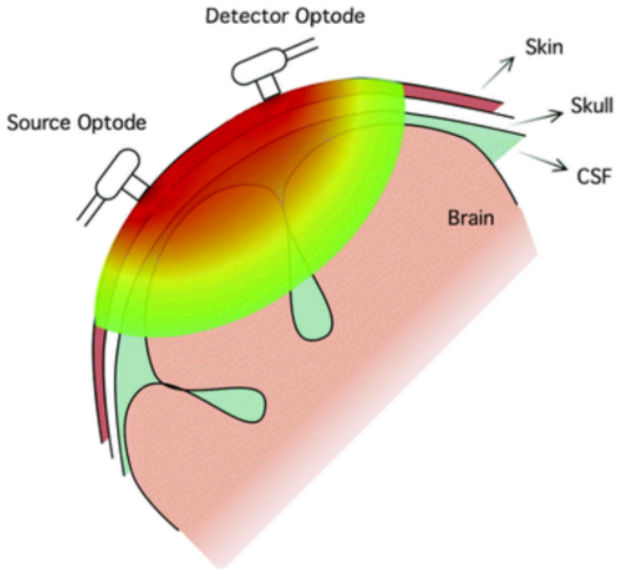

Figure 2.2: Illustration of a typical measurement of the brain using diffuse light.[34]

An implementation of such a time-gated system spread structed by selb et al. in 2005[27], where the researchers measured the intensity of a 500 ps time gate with a fast electronic shutter at seven

different time delays. The measurements can also be used to reconstruct the TPSF.

Another more popular method of measuring the TPSF is the time-correlated single photon counting (TCSPC) technique. A computer records the photon's time of flight in a histogram. This process is repeated until a sufficient number of photons have accumulated to reconstruct the TPSF's shape in the histogram, which is shown in the figure2.3..

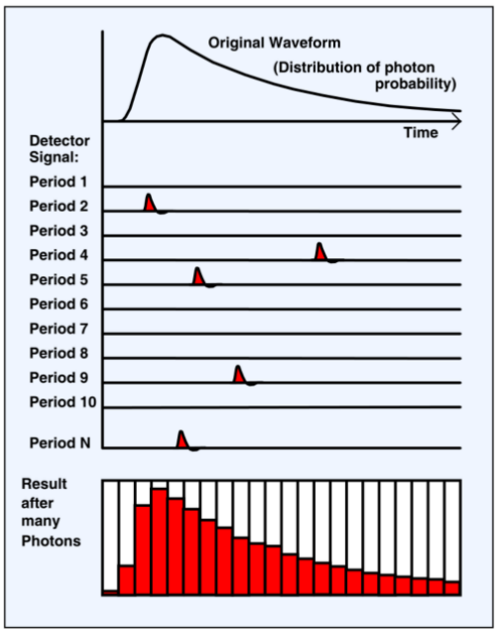

Figure 2.3: Illustration of a typical measurement of the brain using diffuse light.[34]

.

2.2. Measurement using coherent light

NIRS relies on measurements of the average intensity of light, not its coherence properties. DCS uses the coherence of light as a metric for dynamic properties of the medium such as flow and Brownian motion.

2.2.1. Interference and Coherence

Prior to presenting the theory of DCS, it is essential to provide an overview of the fundamental optics related with this concept.

Interference

The interference theory of optics is based on the theory of linear superposition of electromagnetic fields. According to the principle of linear superposition, the electric field E produced by several different

electromagnetic sources at a point in a vacuum is equal to the vector sum,

$$E = E_1 + E_2 + E_3 + \ldots, \tag{2.8}$$

where the E_1, E_2, E_3,... are the electric fields separately generated by the different sources at that point. Consider two series of plane harmonics of the same frequency ω with electric fields,

$$\tilde{E_1}(x,t) = E_{01}e^{i(kx-\omega t+\phi_1)} \tag{2.9}$$

$$\tilde{E_2}(x,t) = E_{02}e^{i(kx-\omega t+\phi_2)} \tag{2.10}$$

where the quantities ϕ_1 and ϕ_2 are introduced to donate any phase difference between the two wave sources. The two waves are said to be mutually coherent if the difference of the phases $\phi_1 - \phi_2$ is constant.
Here we will discuss monochromatic waves that are mutually coherent. From the previous discussion, we know that the irradiance, also known as the intensity of the light, is proportional to the square of the amplitude of the field, then we can write,

$$I = \frac{\langle \tilde{E}\tilde{E}^* \rangle}{2\eta} = \frac{\langle \tilde{E_1}\tilde{E_1}^* \rangle + \langle \tilde{E_2}\tilde{E_2}^* \rangle + \langle \tilde{E_1}\tilde{E_2}^* \rangle + \langle \tilde{E_2}\tilde{E_1}^* \rangle}{2\eta} \tag{2.11}$$

$$= \frac{E_{01}^2 + E_{01}^2 + 2E_{01}E_{02}cos(\phi_1 - \phi_2)}{2\eta} \tag{2.12}$$

$$= I_1 + I_2 + I_{12} \tag{2.13}$$

where I_{12} is called the interference term, this term can make I larger or smaller than the sum of the intensities, depending on the phase difference $\phi_1 - \phi_2$.

Coherence

In the following discussion, we assume that all quantities are stable. And for simplicity, the polarisation states of the two light fields are assumed to be the same in order to ignore the vectorial nature of the light fields. We assume a simplified diagram of the light range in an interference experiment, taking t to be the time required for one light signal to pass through the transverse path 1 and t + τ to be the time required for another light signal to pass through the transverse path 2, the interference term in the intensity equation for light can be written as,

$$2Re\Gamma_{12}(\tau) \tag{2.14}$$

where,

$$\Gamma_{12}(\tau) = \langle E_1(t)E_2^*(t+\tau) \rangle \tag{2.15}$$

The function is called the mutual correlation function or correlation function of the two fields. And the autocorrelation function, also called the self-correlation function, is written as,

$$\Gamma_{11}(\tau) = \langle E_1(t)E_1^*(t+\tau) \rangle \tag{2.16}$$

Sometimes it is more convenient to use a normalised correlation function, also known as the degree of partial coherence. At this point, the peak is 1.

$$\tilde{\gamma}_{11}(\tau) = \frac{\tilde{\Gamma}_{11}(\tau)}{\tilde{\Gamma}_{11}(0)} = \frac{\langle \tilde{E}(t+\tau)\tilde{E}^{\square}(t)\rangle}{\langle \tilde{E}(t)\tilde{E}^{\square}(t)\rangle} \tag{2.17}$$

Note that this is a complex quantity. For example, the degree of coherence of a monochromatic wave is,

$$\gamma_{11} = e^{-i\omega\tau} \tag{2.18}$$

In general, the function a is a complex periodic function of τ, if a is not 0 will produce interference fringes, coherence has the following types,

$$|\gamma_{12}| = 1 \qquad (complete \quad coherence) \tag{2.19}$$

$$0 < |\gamma_{12}| < 1 \qquad (partial \quad coherence) \tag{2.20}$$

$$|\gamma_{12}| = 0 \qquad (complete \quad incoherence) \tag{2.21}$$

In reality, there is no absolute monochromatic light, no matter how good the monochromaticity of the light there is a certain spectral width, called quasi-monochromatic light. As light waves are discontinuous, but consist of many wave trains of finite length, the phase between wave trains is random, so the same beam, with different time delays, has different coherence.

Coherence time is a concept related to the length of the wave train. The longer the coherence time, the longer the wave train, and the narrower the spectrum resulting from the Fourier transform, the better the monochromaticity. The nature of quasi-monochromatic light is that the vibration and its resulting field change sinusoidally for a certain time τ_0, after which the phase changes abruptly.

The τ_0 is called the coherence time, and for electromagnetic waves, the coherence time is the time at which a propagating wave (especially a laser or excitation beam) can be considered coherent, which means that its phase average is predictable.

The coherence length, on the other hand, is the distance over which a coherent wave (e.g. an electromagnetic wave) propagates to maintain a specified degree of coherence. In an interference experiment, for interference fringes to be seen, the difference in optical range between the two beams must be no greater than the value,

$$c\tau_0 = l_c \tag{2.22}$$

The quantity l_c is the coherence length.

In the actual atom being emitted, the time between collisions is not constant, so in a more realistic situation, we can define the coherence time as the average of the individual coherence times. The same applies to the coherence length.

2.2.2. Dynamic Light Scattering(DLS) and Diffuse wave spectroscopy(DWS)

Dynamic Light Scattering(DLS), which is also called quasi-elastic light scattering (QELS) or photon

correlation spectroscopy (PCS), The original form of DLS is to estimate particle size in the solution by measuring its diffusivity or diffusion constant D_B. In biological applications, it can also be called Laser Scattered Contrast Imaging (LSCI)[9].In the DLS technique, it is assumed that light is only scattered once as it passes through the sample. Because of the Doppler effect, the scattered light waves are frequency-shifted to different frequencies, depending on the direction and speed of the particle's motion. As a result, the spectrum widens and the light becomes less coherent.

Another explanation is from the intensity autocorrelation function. If a particle is stationary, the scattered field from one particle is in a different phase from the others and therefore produces an interference pattern in the far field, which is also known as a scattering pattern. However, in fact, the distance between particles in solution varies continuously with time as the small particles in suspension undergo Brownian motion. Then we assume that the particle is moving and observe a single point in the pattern. The intensity of this point will fluctuate due to the change in phase caused by the motion of the particle. A change in phase difference will change the interference pattern. If we record the change in intensity of the three shifts with time, we can learn the correlation between the intensity at t and t+τ. This property can be quantified by having an autocorrelation function.

The figure2.4 shows an interference pattern in the far field known as a speckle pattern.

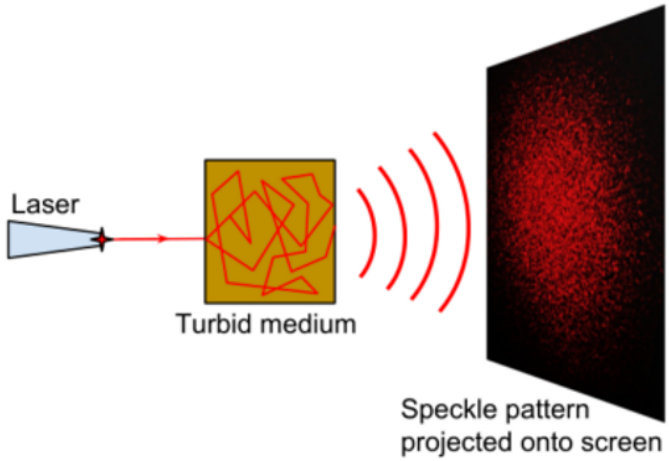

Figure 2.4: Speckle Pattern[34]

Time-varying scattering and Doppler methods are different ways of looking at the same phenomenon, and both techniques measure at a single point[5]. Although we can measure the spectrum directly, modern instruments offer better resolution by making measurements in the time domain, so we will discuss the time-varying intensity of the scattering characterised by the autocorrelation function. Denote the non-normalized field autocorrelation function by G_1,

$$G_1(\tau) = \langle E(t)E^*(t+\tau)\rangle \tag{2.23}$$

where the $E(t)$ is the complex amplitude of the field, for isotropic independent particles, the normalized electric field temporal autocorrelation function $(g1)$ at the detector is,

$$g_1(\tau) = \frac{G_1(\tau)}{G_1(0)} = \frac{\langle E(t)E^*(t+\tau)\rangle}{\langle E(t)E^*(t)\rangle} \tag{2.24}$$

In fact, the data detected by the detector is the intensity, so we can obtain the non-normalized intensity autocorrelation function G_2,

$$G_2(\tau) = \langle I(t)I(t+\tau)\rangle \tag{2.25}$$

Therefore, the normalized intensity autocorrelation function is,

$$g_2(\tau) = \frac{G_2(\tau)}{G_2(0)} = \frac{\langle I(t)I(t+\tau)\rangle}{\langle I(t)\rangle^2} \tag{2.26}$$

According to the Siegret relation[6],

$$g_2(\tau) = 1 + \beta|g_1(\tau)|^2 \tag{2.27}$$

where β is a correction factor that depends on the geometry and alignment of the laser beam in the light scattering setup, and under some certain, this relation can be written as,

$$g_2(\tau) = 1 + |g_1(\tau)|^2 \tag{2.28}$$

The simplest way to measure intensity autocorrelation is to record the scattered light directly, with the detector outputting a current proportional to the intensity of the light hitting the detector, and the intensity autocorrelation can then be calculated from the measured intensity over time. At lower light intensities, photon counting can also be used, where the detector outputs a pulse when a single photon is detected.

Diffuse wave spectroscopy(DWS) was also originally studied in the context of particle motion and size, like DLS. DWS technology has been used to study the collective dynamics of materials[17], food science[8], biomedical applications[26], and other fields.

DWS eliminates the assumption that light is only scattered once from a medium and complements DLS, which posits that light's firm multiple scattering limits and propagation through tissue may be described as a scattering process. DWS, like DLS, captures the light intensity from individual scattering sites over time and measures the autocorrelation function. The distinction is that DWS does not have a well-defined scattering angle due to multiple scattering. Furthermore, the angular dependency and polarisation properties of scattered light in turbid media are hidden, and the dynamic parameters of the medium have an intensity characterization of the scattered light. Furthermore, in contrast to DLS, DWS measurements are sensitive to fluctuations in the medium on length scales much smaller than the wavelength of light and these fluctuations can be detected on a very wide range of time scales[17].

The basic experimental setup of DLS and DWS are shown in figure2.5. A coherent light wave impinges a volume and is scattered to all directions. The detector is placed at an angle θ from the light path of the light source to measure the scattered light in DLS, while there is no certain scattering angle in DWS.

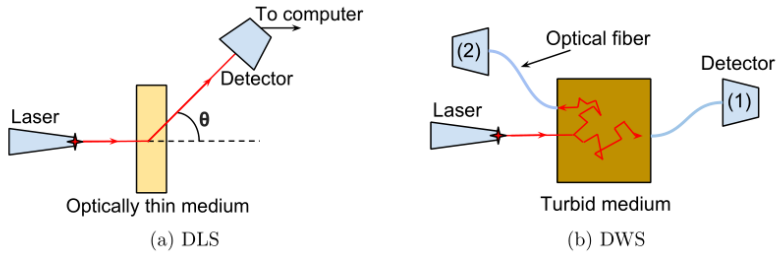

Figure 2.5: (a) Experiment schematic for DLS.(b) Experiment schematic for DWS[34].

2.2.3. Diffuse Correlation Spectroscopy(CW-DCS)

Continuous wave diffuse reflectance correlation spectroscopy(CW-DCS), like DLS and DWS, uses a continuous wave laser source. This technique is often referred to in the literature simply as ”DCS”, but is also referred to as ”CW-DCS” in order to distinguish it from time-domain diffuse correlation spectroscopy. In fact, ’diffuse correlation spectroscopy’ is a renaming of DWS.

The term ’DCS’ has become the term used in the field because it better describes the underlying signal acquisition process which relies on diffuse photon correlation.

Studies of depth-resolved DCS [34] have shown that normalized electric field autocorrelation functions for different path lengths can be obtained by,

$$g_1(\tau, s) = exp(-\frac{1}{3}k^2\langle\Delta r(\tau)^2\rangle\frac{s}{l^*}) \tag{2.29}$$

where s is a photon’s path length, k is the wavenumber of light, $\langle\Delta r(\tau)^2\rangle$ is the average displacement squared of the scatters in time τ, and l^* is the transport mean free distance (TMFP).
For a long time, red blood cells were considered to be in Brownian motion rather than random flow due to the multiple scattering of red blood cells in different vessels[4]. For Brownian motion,

$$\langle\Delta r(\tau)^2\rangle = 6D_B\tau \tag{2.30}$$

Where D_B is the Brownian Motion coefficient, so g_1 can be written as,

$$g1(\tau, s) = exp(-2\mu'_s k^2 D_B s\tau) \tag{2.31}$$

Modern iterations of CW-DCS use a different form of theory from that presented in the previous section, although the solutions are largely the same. the assumptions made in DWS theory are too restrictive and in some cases do not fully explain the experimental data, such as the backscattering geometry. In 1992, Ackerson et al. proposed an approach that suggested that, mathematically, correlations are transported through the medium in the same way as light, and proposed a correlation transport (CT) equation, which is similar to the radiative transport equation(RTE), which will be discussed in the subsequent discussion. Under certain conditions, this approach can be simplified to the single scattering theory of DLS and the multiple scattering theory of DWS, and can also use the same mathematical tools as for radiation transport, making it more widely applicable.

2.2.4. Time-Domain Diffuse Correlation Spectroscopy(TD-DCS)

TD-DCS uses laser pulses as a light source and simultaneously measures TPSF and autocorrelation, which are similar to TD-NIRS and pulsed DWS. We can then use the photon scattering theory developed for TD-NIRS to directly estimate tissue optical properties. Therefore, a large portion of the error in estimating dynamical properties caused by imprecise optical property values is eliminated[31].

For TD-DCS, the photon time of flight(TOF) and the absolute time of arrival are recorded, where the TOF histogram makes it possible to calculate the TPSF and estimate the optical properties. The absolute arrival time allows us to calculate autocorrelation functions and estimate dynamic properties.

And the third advantage is from time-gating techniques. By using time-gating techniques, the dynamics of particular layers of interest can be estimated.
Figure2.6 shows the conceptual illustration of time-domain diffuse correlation spectroscopy.

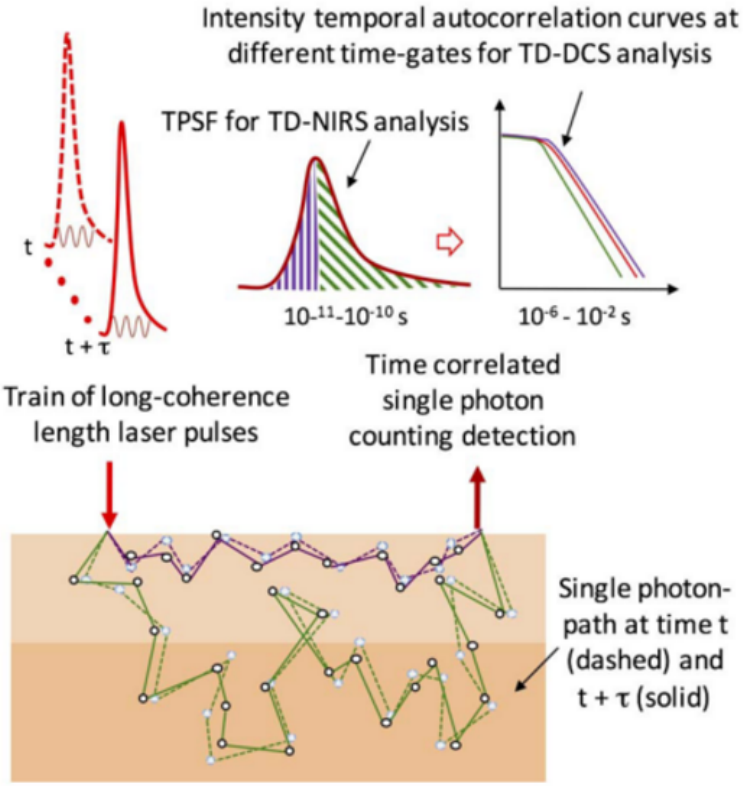

Figure 2.6: Illustration demonstrating the concept of time-domain diffuse correlation spectroscopy[31].

2.3. Modeling light transport

Analysis of photon transport in biological tissues can be carried out either by numerical modeling through Monte Carlo simulations or by the radiative transfer equation (RTE). However, solving the RTE requires the introduction of approximations and a common approximation is the diffusion approximation. Overall, the solution to the photon transport diffusion equation is more computationally efficient but not as accurate as Monte Carlo simulations[38].

2.3.1. Diffusion Theory

radiative transfer equation (RTE)

The application of radiative transfer theory to describe the propagation of light in turbid media has met with greater success. In the RTE form, light propagation is treated as a flow of discrete photons which are absorbed or scattered by the medium. This theory only explains the transmission of light energy, ignoring the amplitude and phase of the wave, as well as diffraction, interference, and polarisation.

The diffusion approximation (DA) is a widely used method that employs the Radiative Transfer Equation (RTE) as a model to describe the forward propagation of photons[29]. In terms of computational efficiency and accuracy, the diffusion approximation offers significant advantages, due to these advantages, it has been widely employed and is now the foundation for many applications based on data analysis theory.

The RTE can mathematically model the transfer of energy as photons move through the tissue and can be derived from the law of conservation of energy. the RTE states that a beam of light loses energy through absorption and scattering away from the beam, and gains energy from scattering from the light source and pointing beam[38]. Assuming that the scattering is elastic, the RTE can be written as,

$$\frac{1}{v}\frac{\partial L(r,t,\hat{s})}{\partial t} + \hat{s}\cdot\nabla L(r,t,\hat{s}) = -(\mu_a+\mu_s)L(r,t,\hat{s}) + \mu_s\int_{4\pi} L(r,t,\hat{s})P(\hat{s},\hat{s'})d\Omega + S(r,t,\hat{s}) \tag{2.32}$$

In this equation, the light radiance $L(r,t,\hat{s})$ is the core dependent variable quantity which will be simulated in this report, which is defined as the light power unit area traveling in the direction of $\hat{s}$ at the position **r** and time t.

A P_N approximation can be employed to reduce the complexity of the RTE(2.32). In this method, L is Written as a series expansion of spherical harmonies $Y_{lm}(with \quad coefficient \quad \phi_{lm})$ which is truncated at l=N[13]:

$$L(r,t,\hat{s}) = \Sigma_{l=0}^{N}\Sigma_{m=-l}^{l}\sqrt{\frac{2l+1}{4\pi}}\phi_{lm}(\mathbf{r},t)Y_{lm}(\hat{s}) \tag{2.33}$$

When $L(r,t,\hat{s})$ is nearly isotropic,the P_1 approximation, where N=1, is valid, then the equation can be written as

$$L(r,t,\hat{s}) = \frac{1}{4\pi}\Phi(\mathbf{r},t) + \frac{3}{4\pi}\mathbf{J}(\mathbf{r},t)\cdot\hat{s} \tag{2.34}$$

In the equation2.34, $\Phi(\hat{r},t)(W\cdot cm^{-2})$ is the photon fluence rate, and $\mathbf{J}(\mathbf{r},t)(W\cdot cm^{-2})$ is the photon flux,

$$\Phi(\mathbf{r},t) = \int_{4\pi} L(r,t,\hat{s})ds = \phi_{00} \tag{2.35}$$

and,

$$\begin{aligned}\mathbf{J}(\mathbf{r},t) &\equiv \int_{4\pi} L(r,t,\hat{s})\hat{s}ds \\ &= \frac{1}{\sqrt{2}}(\phi_{1-1}-\phi_{11})\hat{y} + \phi_{10}\hat{z}\end{aligned} \tag{2.36}$$

$\mathbf{J}(\mathbf{r},t)\cdot\hat{s}$ is the power per area traveling in the direction of $\hat{s}$ at the position **r** ant time t.

A continuity equation derived from integrating equation (1) over all solid angles relates photon fluence rate and flux,

$$\frac{1}{v}\frac{\partial\Phi(\mathbf{r},t)}{\partial t} + \nabla\cdot\mathbf{J}(\mathbf{r},t) + \mu_a\Phi(\mathbf{r},t) = S(\mathbf{r},t) \tag{2.37}$$

Where $S(\mathbf{r},t)$ S(r,t) denotes the total power per volume radially radiated from position **r** at time t. Substitute Eq.2.33 into Eq. 2.32 and assuming an isotropic light source, the Fick's law of diffusion can be obtained,

$$\nabla\phi(\mathbf{r},t) = -3(\mu_a + \mu_s^{'})\mathbf{J}(\mathbf{r},t) \tag{2.38}$$

Then, the photon diffusion equation for the photon fluence rate can be written as[13],

$$\nabla(D(\mathbf{r})\nabla\Phi(\mathbf{r},t)) - \mu_a(\mathbf{r})\Phi(\mathbf{r},t)) - \frac{\partial(\mathbf{r},t)}{\partial t} = -S(\mathbf{r},t) \tag{2.39}$$

Where D is the diffusion coefficient, which is defined as,

$$D = \frac{1}{\mu_s^{'}} \tag{2.40}$$

It is worth noting that in turbid samples such as biological tissue, the scattering time is much more than the absorption event, i.e., $\mu_s' \gg \mu_a$, in which case the diffusion equation can approximate the radiation transport equation.

Another assumption in applying diffusion theory to RTE is that the time for a substantial change in current density in the main scattering medium is much longer than the time to traverse a transmission-mean free range. This assumption also requires the medium to be turbid.

Therefore, the assumptions required to characterize photon behavior by the diffusion equation introduce uncertainties, and as the absorption coefficient increases and the scattering coefficient decreases, the propagation of light through the medium no longer meets the precondition that there are far more scattering events than absorption events, the diffusion approximation will become less accurate[39]. Concerning the errors in the application of diffusion theory to calculations, Lihong VWang and his team showed that diffusion theory and similarity relations can provide accurate results when the photon source is isotropic and deep enough in the medium[30]. These conclusions have inspired a new theory combining Monte Carlo simulations and diffusion theory called the hybrid model[37].

In practical applications, many situations of interest involve different types of light sources, tissue sample types and complex illumination geometries. It is often necessary to make assumptions about the parameters and boundary conditions involved to obtain an analytical equation for the RTE. However, in such cases, even if an analytical solution can be obtained, it is still very complex.

Correlation transfer equation (CTE)

DCS uses the coherence of light as a metric for dynamical properties of the medium such as flow and Brownian motion.

Formally, DCS relies on the fact that the temporal correlation of light fields in turbid media also obeys the diffusion equation, albeit differently from that used for absorption and diffusion spectroscopy.

It has been suggested that correlations are also transmitted through the medium, which is similar to light transport,The steady-state equation is,

$$\nabla \cdot G_1^T(\mathbf{r}, \hat{s}, \tau)\hat{s} + (\mu_a + \mu_s)G_1^T(\mathbf{r}, \hat{s}, \tau) = \tag{2.41}$$

$$Q(\mathbf{r}, \hat{s}) + \mu_s \int G_1^T(\mathbf{r}, \hat{s}^{'}, \tau)g_1^s(\hat{s}, \hat{s}^{'}, \tau)f(\hat{s}, \hat{s}^{'})ds^{'} \tag{2.42}$$

This equation is valid for CW sources and equilibrium systems

$$\nabla(D(\mathbf{r})\nabla G_1(\mathbf{r}, \tau)) - (\mu_a(\mathbf{r}) + \frac{\alpha}{3}\mu_s^{`}k_0^2\langle\Delta\mathbf{r}^2(\tau)\rangle)G_1(\mathbf{r}, \tau) = S(\mathbf{r}, \tau) \tag{2.43}$$

The advantage of this formulation is that it not only reduces to the single-scattering theory of DLS and the multiple-scattering theory of DWS under suitable conditions, but it also allows the correlation to be analyzed using the same mathematical tools as the radiation transport equation, which has broader applicability.

The diffusion approximation mentioned above of the RTE can be employed as such a mathematical method. Similarly, the appropriate transport equation in a turbid fluid can be approximated as the applicable diffusion, which is

$$(-\frac{1}{3\mu_s^{`}}\nabla^2 + \mu_a + 2\mu_s^{`}k_0^2\alpha D_B\tau)G_1(r, \tau) = S(r) \tag{2.44}$$

Comparing this with the light diffusion equation, it can be seen that in addition to the absorption term μa, we have a ”correlated absorption” term $2\mu_s^{`}k_0^2\alpha D_B\tau$, which explains the decrease in correlation during ”correlated diffusion”.

Because this approximation employs the same formal and mathematical technique as the RTE’s diffusion approximation described in the preceding section, the conditions of applicability and advantages and disadvantages of the CTE’s diffusion approximation are also the same.

2.3.2. Finite Element Simulations

The finite element method (FEM) is a popular numerical method for solving differential equations in engineering and mathematical modeling. It can be used to solve the light density diffusion equation. To mathematically model a physical problem using this method, certain assumptions must be made, resulting in differential equations that control the mathematical model. Finite element analysis provides an approximate solution to this model. Because the finite element method is a numerical technique, it is important to assess the accuracy of its solutions[19].

To introduce the progress of using FEM to simulate light transport, we start with the diffusion approximation mentioned in previous section, and write it in the frequency domain,

$$-\nabla \cdot \kappa(r)\nabla\Phi(r, \omega) + (\mu_a(r) + \frac{i\omega}{c_m(r)})\Phi(r, \omega) = q_0(r, \omega) \tag{2.45}$$

This diffusion equation in the FEM framework can by written as a system of linear algebra equations,

$$(K(\kappa) + C(\mu_a + \frac{i\omega}{c_m}) + \frac{1}{2A}F)\Phi = q_0 \tag{2.46}$$

Where the matrices $K(\kappa)$, $C(\mu_a + \frac{i\omega}{c_m}$ and F are,

$$K_{ij} = \int_\Omega \kappa(r)\nabla u_i(r) \cdot \nabla u_j(r) d^n r \tag{2.47}$$

$$C_{ij} = \int_\Omega (\mu_a(r) + \frac{i\omega}{c_m(r)}) u_i(r) u_j(r) d^n r \tag{2.48}$$

$$F_{ij} = \oint_{\partial\Omega} u_i(r) u_j(r) d^{n-1} r \tag{2.49}$$

and the source vector q_0 has terms,

$$q_{0_i} = \int_\Omega u_i(r) q_0(r) d^n r \tag{2.50}$$

FEM simplifies the radiative transport equation by assuming isotropic light transport. The advantage of this method is its computational efficiency, providing accurate results at regions distant from the light source. However, the implementation of the FEM can be technically demanding and its accuracy is limited in proximity to the light source[33].

One example of FEM-based simulation is the Near Infrared Fluorescence and Spectral Tomography (NIRFAST), which provides a comprehensive modelling and image reconstruction framework for single- and multi-wavelength optical or functional imaging. NIRFAST utilizes FEM to simulate the propagation of light through biological tissues.Figure 1 shows a flow chart indicating the specific commands within the software package NIRFAST. The previous studies have shown that NIRFAST is capable of 2D and 3D examples of single-wavelength as well as multi-wavelength spectral modelling and image reconstruction[10]. Figure 2.7 depicts the flowchart that demonstrate the particular commands of the software package NIRFAST, as well as the overall structure of the routines.

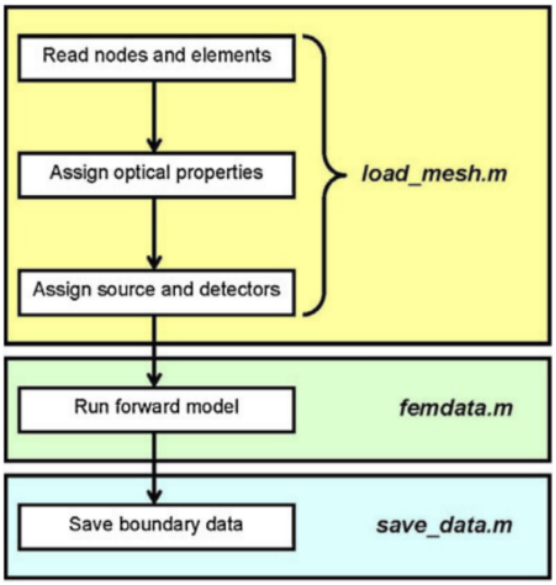

Figure 2.7: Flowchart of the sequence and commands used in NIRFAST for a generalized forward model[10].

Another example is using COMSOL Multiphysics (Version 5.4a)[35]. In this research, we use finite elemental method (FEM) to construct microvascular bilayer skin tissue progression. What kind of time-related light scattering method and generated point light source illumination sum-correlation diagram. In addition, computer analysis was performed to clarify the accompanying skin surface blood flow velocity, hair vessel depth change, and BFI-like change.

The results of this study show that BFI shows proportional changes in the inlet blood flow velocity through the capillaries but does not vary significantly with capillary depth.

2.3.3. Monte Carlo Simulation

Monte Carlo simulation is a fundamental and general method for modeling light in tissue. In the typical MC modeling process, the movement of light within tissue is simulated by following the random path taken by photon packets as they move through a modeled tissue[40]. Because Monte Carlo simulation is applicable to arbitrary 3D configurations of tissue properties and source-detector localization, it is considered the 'gold standard' of modeling. As the Monte Carlo model is not involved in this paper, only a brief overview is given.

For cases where an analytical solution of RTE cannot be obtained, numerical techniques can be used to solve the problem. Photon migration based on Monte Carlo simulation methods is the most widely used method[28],such as an application using Monte Carlo Model to solve radiative transfer equations in biological tissues [23].

The figure2.8 shows an example of Monte Carlo Simulation for photon migration.

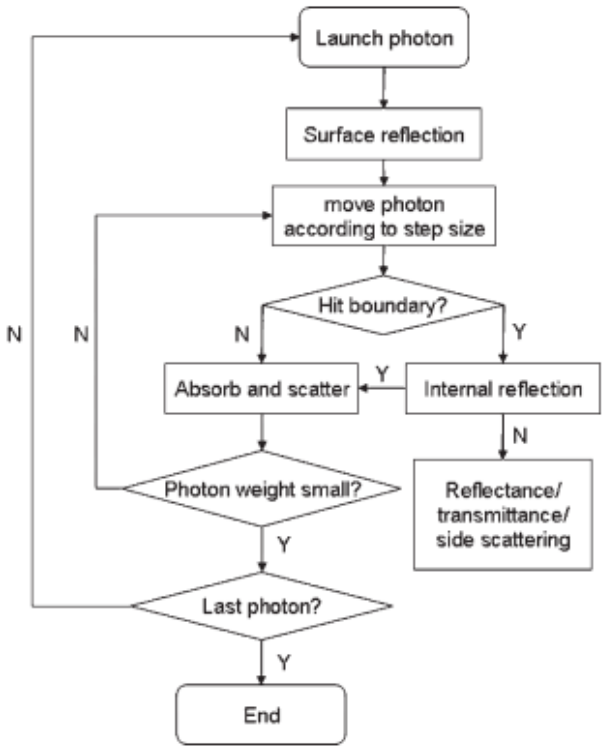

Figure 2.8: Schematic diagram of Monte Carlo simulation of photon migration[36].

One of the critical points in MC simulations is defining a new photon direction after each scattering event. One of the most popular solutions is to use the Henyey-Greenstein phase function [2].

In the biomedical field, there are already many teams applying Monte Carlo simulations to solve practical problems[9]. Utilizing the Monte Carlo (MC) approach in the context of photon migration presents several notable benefits□ including effective modeling of light in turbid media, simple simulation algorithms, versatility for real-world transport, and compatibility with any albedo and SPF.[28].

However, there are disadvantages to using Monte Carlo simulations for photon migration analysis. To get a statistically significant result we have to get a lot of data, which means we have to track millions of photon tracks, so Monte Carlo simulations can be very slow, and a Monte Carlo simulation can take hours or even days.

2.4. Summary

The main objective of this chapter is to present a comprehensive overview of the essential concepts associated with diffuse optics.

Additionally, it gives a concise introduction to the concepts of near-infrared spectroscopy (NIRS) and diffuse correlation spectroscopy (DCS). Furthermore, this section also introduces frequently utilized methodologies for simulating light transmission, including diffusion theory, finite element methods, and Monte Carlo simulations. These theoretical foundations underpin the fundamental research content of this paper.

3

Case Study: Simulation of RTE

The primary objective of this chapter is to examine the application of the finite element method in simulating the diffusion equation for the radiative transfer equation (RTE). As previously stated, the Radiative Transfer Equation (RTE) can quantitatively represent photons' energy transfer as they propagate through biological tissue. In certain circumstances, diffusion theory can effectively approximate the RTE, leading to the derivation of the diffusion equation.

This chapter aims to investigate the research questions presented in Chapter 2, specifically addressing the validity of the diffusion approximation equation in modeling the Radiative Transfer Equation (RTE) using a finite element model. What impact will variations in model parameters exert on the outcomes of the simulation? This section of the study comprises multiple components. The focus of this study pertains to the development and refinement of models, the curve fitting of data, and the comprehensive analysis and summarization of errors. Furthermore, this paper examines possible factors contributing to the occurrence of errors.

3.1. Problem

The utilization of diffusion approximation for solving the radiation transport equations is extensively employed due to its notable benefits in terms of computational efficiency and precision. This section aims to develop a concise and effective finite element model for the simulation of the Radiative Transfer Equation (RTE) using the diffusion approximation. Furthermore, the objective is to investigate model parameters' impact on the simulation outcomes' accuracy and reliability.

The fundamental form of geometry is single-layer geometry, as depicted in Figure 1, which illustrates the geometry employed in solving the Radiative Transfer Equation (RTE) within this context.

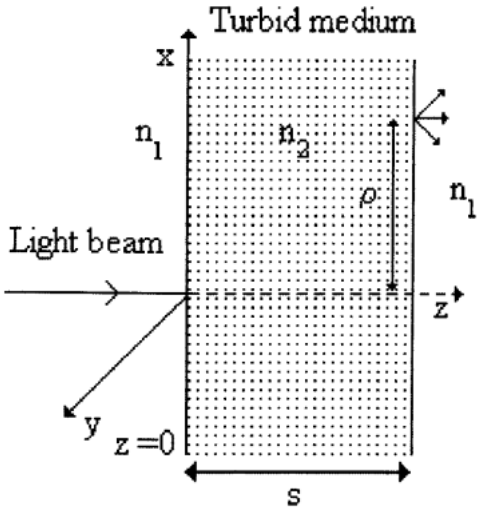

Figure 3.1: Geometry of the Simulation[7]

Set $\rho = 0$ while solving the transmission. And set the light source according to the simulation needs.

An important assumption mentioned before for employing the diffusion approximation to solve the Radiative Transfer Equation (RTE) is that the detection point is sufficiently distant from the boundary, ensuring its ”deep enough” placement. Hence, an investigation is conducted to examine the impact of the distance from the boundary, namely the plate geometry's thickness, on the solution's precision. The concept of ”infinity” is considered an ideal assumption, and in the simulations, the width is intentionally set to a significantly greater value than the thickness. This is done to mitigate the potential impact of width on the results.

Furthermore, defining the mesh is a crucial step within the realm of finite element analysis. Therefore, this chapter will also examine the impact of mesh dimensions.

3.2. Methodology

The **Coefficient Form PDE** provides a general interface for specifying and solving numerous well-known partial differential equations in coefficient form. Many partial differential equations from physics and other domains can be converted into a generic form with second-order derivatives in time and space. Such partial differential equations can be defined in COMSOL Multiphysics by setting the coefficients of different orders of derivatives. The model was executed on the TU Delft cluster due to the constrained computational capabilities of home computers.

To determine the parameters μ_a and $\mu_s^{'}$ for a given tpsf, one can employ a fitting algorithm. Additionally, it is possible to investigate the simulation method and compare its outcomes with the analytical solution. This comparison allows for an examination of the error magnitude and the trend of change between the simulation results and the analytical solution. Furthermore, an analysis of the potential causes for the observed error can be conducted. It is important to acknowledge that the amplitude of the curves is contingent upon time, necessitating the normalization of the curves throughout subsequent fitting procedures. It is noteworthy to mention that the conditions employed in the analytical

solution correspond to the conditions simulated in the COMSOL model.

The least squares approach is a widely used technique in regression analysis. It aims to find the best approximation for the solution of overdetermined This is achieved by minimizing the sum of the squared residuals in each equation's outcome. The primary application of this method is in fitting data to a model. The formal discovery and publication of the method of least squares is attributed to Adrien-Marie Legendre.[24].

The **lsqcurvefit** in MATLAB is a computational tool utilized for solving nonlinear curve fitting issues by the method of least squares, the basic function is,

$$\min_x ||F(x, data) - ydata||_2^2 = \min_x (F(x, xdata_i) - ydata_i)^2 \tag{3.1}$$

The coefficient x of the problem is determined by solving a function that involves constructing an equation and data, as well as defining the input data xdata and output data ydata inside the dataset.

3.3. Simulation

The Helmholtz equation is used to solve the flunce rate $\Phi(r,t)$

$$\nabla\cdot(D(r)\nabla\Phi(r,t))-\mu_a(r)\Phi(r,t)-\frac{\partial\Phi(r,t)}{v\partial t} = -S(r,t) \tag{3.2}$$

Where S is the source term[32],

$$S = \frac{1}{4\pi^{3/2}}\frac{W_p}{\tau_p}exp(-\frac{4\cdot(t-\tau_c)^2}{\tau_p^2})\delta(r-r_0) \tag{3.3}$$

And μ_a and $\mu_s^{'}$ (with $\mu_s^{'} = \frac{1}{3D}$) are the coefficient which will be fitted while curve fitting, v is the velocity of light in the tissue, which is,

$$v = \frac{c}{n} \tag{3.4}$$

The index of refraction n of biological tissue is about 1.4.

Studies have shown that when the tissue is irradiated with light with a wavelength of around 630nm, the interaction coefficients of mammalian soft tissue are in the range of $0.001mm^{-1} < \mu_a < 0.5mm^{-1}$, $35mm^{-1} < \mu_s < 70mm^{-1}$ and $0.7 < g < 0.99$.[25]. For the values of the diffusion coefficient and absorption coefficient of different tissues, the data from [32] of $\mu_a = 0.021mm^{-1}$ and $\mu_s^{'} = 1.81mm^{'}$ were used to simulate in this report, which were also within this range.

After entering the tissue, the photons travel through the tissue along random walk pathways. Each photon travels through a straight-line segments and its propagation direction changes suddenly and randomly. Meanwhile, some photons are absorbed. The average length of the straight-line segments is defined as the photon random walk step or the transport mean free path (TMFP)[13], z_0, which is

$$z_0 = \frac{1}{\mu_s^{'}} \tag{3.5}$$

The assumption of an isotropic source in the diffusion model is violated when light is directed from a collimated source. In terms of this light source, it is a good approximation to replace it with an isotropic point light source positioned at a specific depth, denoted as z_0 [15].

According to the definition of the absorbing coefficient, the average distance that photons travel in the tissue before being absorbed is l_a, which is[34],

$$l_a \equiv \frac{1}{\mu_a} \tag{3.6}$$

If the size of the mesh is too large, the model will not be able to simulate as well as possible how light is scattered and absorbed in the tissue. Therefore, based on the definitions of z_0 and l_a, it is necessary that the largest value of the mesh size does not exceed the minimum value between these two. In other words, the mesh size must be less than or equal to z_0.

The boundary condition of the model is also necessary to take into account. Near the boundary, the radiation is no longer isotropic. In this case, the diffusion equation must be modified to allow for Fresnel reflection at the interface. Photons typically do not re-enter the tissue after traveling away from the tissue into the air. As a result, the incoming irradiance at the barrier is due to the Fresnel reflection of radiation flowing toward the boundary.

the incoming irradiance J describes the total light power per unit area traveling into the diffuse medium at the boundary[21], which is written as,

$$J_{in} \equiv \begin{cases} \int_{\hat{s}\cdot\hat{n}<0} L(\hat{s})\hat{s}\cdot(-\hat{n})ds, \\ \int_{\hat{s}\cdot\hat{n}>0} R_{Fresnel}(\hat{s})L(\hat{s}\hat{s})\cdot(\hat{n})ds \end{cases}$$

Where $R_{Fresnel}(\hat{s})$ is the Fresnel reflection coefficient for light incident upon the boundary in a direction $\hat{s}$ from within the medium. The partial flux boundary condition, which is also known as Robin boundary condition

$$\phi = z_b\hat{n}\cdot\nabla\phi \tag{3.7}$$

The equation 3.7 shows the fluence rate at the boundary, where the term z_b is the z-coordinate of the boundary, and $\hat{n}$ is a unit normal vector from inside the tisse to outside. z_b is defined as,

$$z_b = \frac{2z_0(1+R_{eff})}{3(1-R_{eff})} \tag{3.8}$$

Where R_{eff} is the effective reflection coefficient that accounts for the index mismatch between the diffusing medium and the air. R_{eff} can be calculated by,

$$R_{eff} = -1.4399 * n^{-1} + 0.7099 * n^{-1} + 0.6681 + 0.0636 * n; \tag{3.9}$$

The extrapolated-zero boundary condition might be considered a more straightforward boundary condition. The flux rate is approximated using a Taylor expansion up to the first order near the border[13].

The first-order derivative term is obtained from the partial flux boundary condition.

$$\Phi(z = -z_b) = 0 \tag{3.10}$$

Using the ”new” zero flux interface facilitates the application of graphical techniques to derive analytical answers for diverse geometrical configurations. The extrapolated zero boundary condition is fulfilled

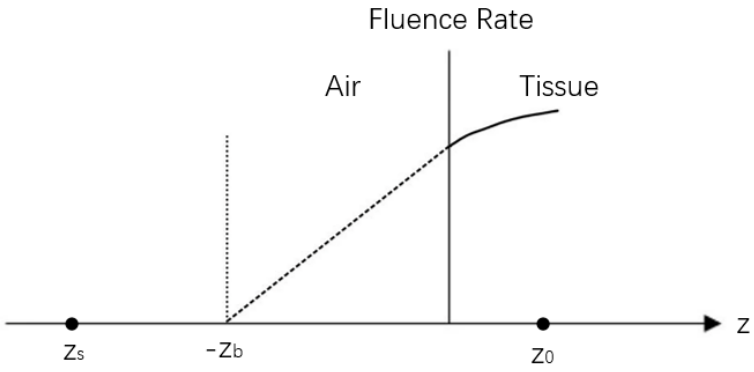

Figure 3.2: Schematic diagram of extrapolating zero boundaries[13]

by introducing a negative image point source at $z_s = -(2z_b + z_0)$ (as depicted in Figure 3.2).

The extrapolated boundary condition suggests that the average diffusion intensity is equivalent to zero at the extrapolated boundary situated beyond the turbid medium, at a distance ze defined by,

$$z_e = 2AD \tag{3.11}$$

where the coefficient A is defined as,

$$A = \frac{(1+R)}{(1-R)}; \tag{3.12}$$

The Figure.3.3 shows that employing the geometry with $L = 1mm$ as an example of the 2D plot,

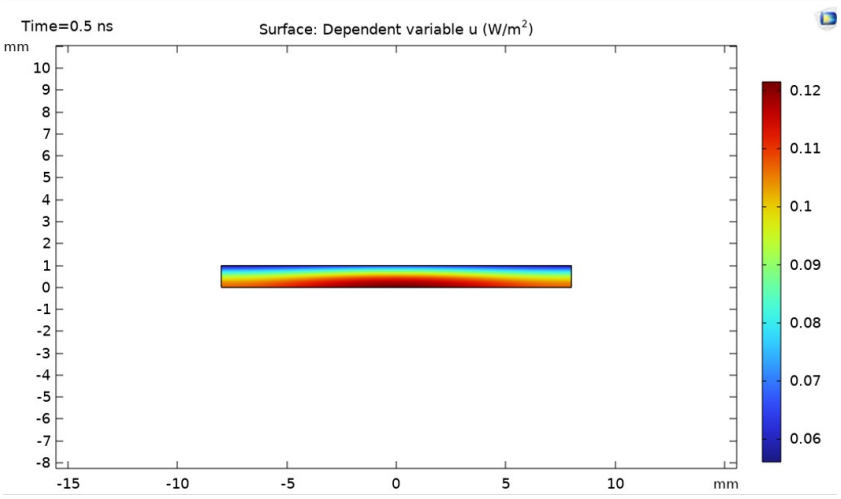

Figure 3.3: Simulation Result

After making adjustments to the geometry and rerunning the model, it can be observed that the 2D

plot depicting the intensity distribution has changed, which is shown in Figure.3.4.

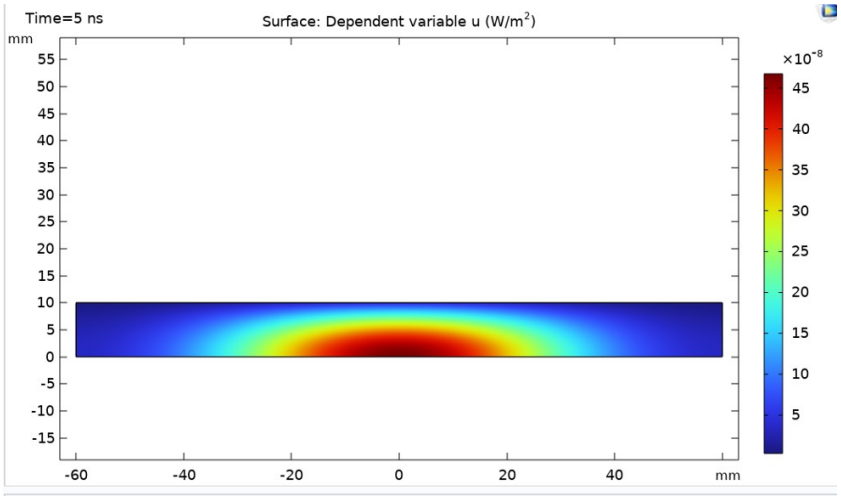

Figure 3.4: Simulation Result with thickness $s = 10mm$

The geometric dimensions research kept the mesh size and the simulated Helmholtz equation constant. The mesh size has a maximum value of 0.1 mm. The thicknesses of the geometry of 2 mm, 5 mm, 10 mm, 20 mm, 30 mm, 40 mm, and 50 mm were chosen for the simulation based on the usual sizes of actual biological tissues, and the data collected from the simulation were fitted to the theoretical function of the fluence rate. Based on the previously discussed approximation of substituting a collimated beam with an isotropic point source located at $z = z_0$, the type of source can be changed by adjusting the position of the point source.

For an isotropic point source, the simulation results with various dimensions is shown in the Figure.3.5.

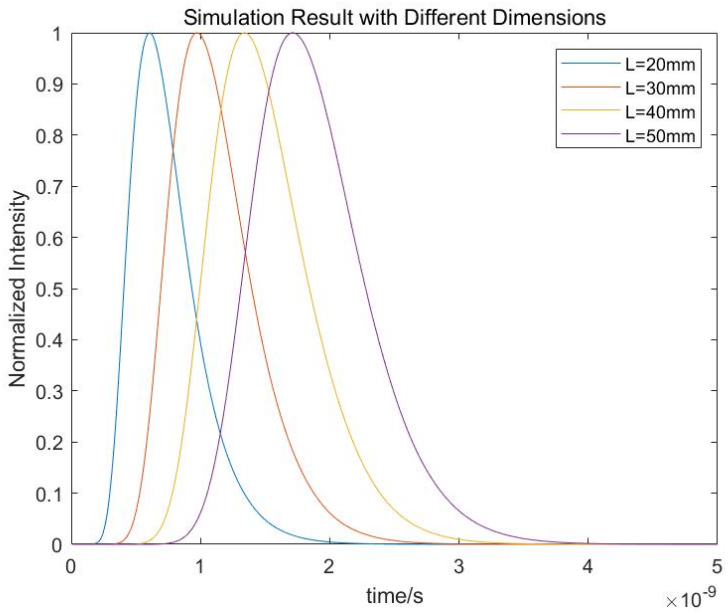

Figure 3.5: Simulation Results When Source is Isotropic Point Source and Thickness Changes

For a collimated beam, simulation results of different thicknesses is shown in Fighre.3.6.

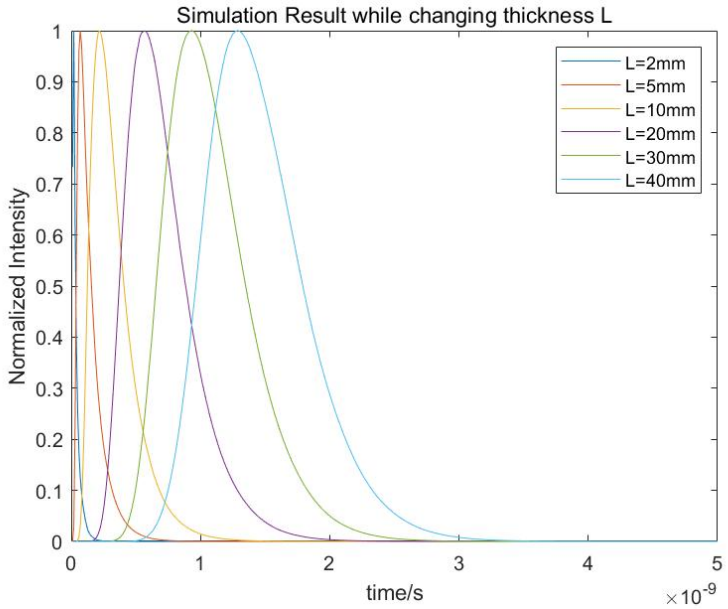

Figure 3.6: Simulation Results When Source is Collimated Beam and Thickness Changes

In order to investigate the impact of mesh dimensions on the simulation outcomes, it is imperative to maintain constancy in the other factors, including geometric dimensions with $L = 20mm$. And as discussed before, the mesh size should be less than or equal to z_0.

Introduce a parameter **meshpara**, with

$$mesh \quad size = \frac{z_0}{meshpara} \qquad with \quad meshpara = 1, 2, 3, 4, 5. \tag{3.13}$$

According to the established definition, an increase in the value of meshpara corresponds to a finer mesh. The results are shown in Figure.3.7, where Figure.3.7a depicts the entirety of the plot while Figure.3.7b provides a more detailed representation of the plot.

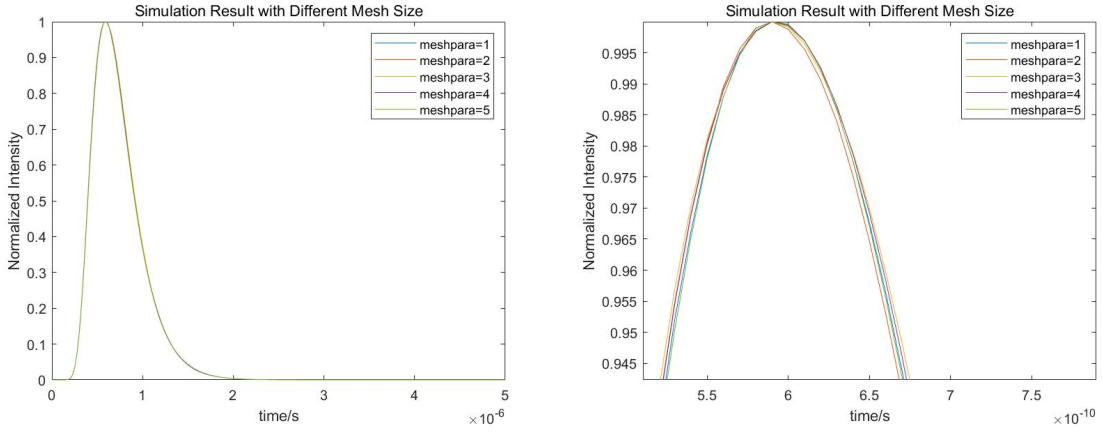

(a) Simulation Results **(b)** Detailed Plot

Figure 3.7: Simulation Results While Changing Mesh Size

The results of curve fitting will be discussed in subsequent sections.

3.4. Curve Fitting

When the light source is a short pulse of light from an isotropic point source, the fluence rate can be written as,

$$\phi = v(4\pi Dvt)^{-3/2} exp(-\frac{r^2}{4Dvt} - \mu_a vt) \tag{3.14}$$

Since the source is a short pulsed laser source, the fitting process commences by inverse convolution of the simulation results with the source term. Plot the simulation results and the analytical solution on one single graph to facilitate comparison, employing the geometric dimension of $L = 20mm$ as an instance, shown in the figure in Figure.3.8.

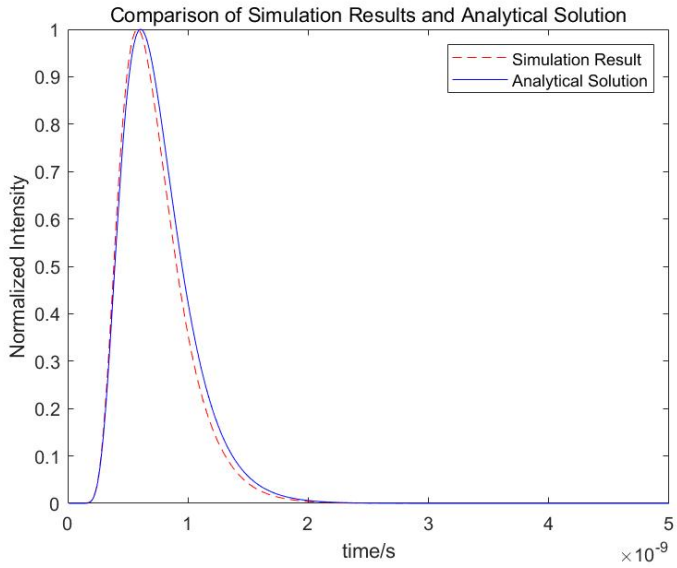

Figure 3.8: Comparison between Simulation Results and Analytical Solution When Source is Isotropic Point Source

When the light source is a collimated beam, the time resolved transmittance is[7],

$$T(\rho, t) = -\hat{q} \cdot \mathbf{F}_d(\rho, z = s, t) = -4\pi D \frac{\partial}{\partial z} U_d(\rho, z = s, t) \tag{3.15}$$

where U_d is,

$$\begin{cases} U_d(z, \rho, t) = U_{d+}(z, \rho, t) + U_{d-}(z, \rho, t), \\ U_{d+}(z, \rho, t) = \dfrac{vexp(-\mu_a vt - \frac{\rho^2}{4Dvt})}{4\pi(4\pi Dvt)^{3/2}} \displaystyle\sum_{m=-\infty}^{m=+\infty} ecp[-\frac{(z - z_{+,m})^2}{4Dvt}], \\ U_{d-}(z, \rho, t) = -\dfrac{vexp(-\mu_a vt - \frac{\rho^2}{4Dvt})}{4\pi(4\pi Dvt)^{3/2}} \displaystyle\sum_{m=-\infty}^{m=+\infty} ecp[-\frac{(z - z_{-,m})^2}{4Dvt}] \end{cases} \tag{3.16}$$

The analytical solution to the diffusion equation involves the utilization of an extrapolated boundary condition. This condition assumes that the average diffuse intensity is zero at a distance of $z_e = 2AD$ from the boundary of the flat plate. This condition can be achieved by employing either an isotropic

point source positioned within the flat plate or by utilizing an unlimited number of dipoles distributed throughout an infinite diffusion medium. Each pair of dipoles corresponds to a combination of positive and negative sources and exhibits identical optical characteristics. Then, the average scattering intensity can be partitioned into two constituents generated by the positive and negative sources. In the expression of U_d, for the positive sources,$z_{+,m}$ and $z_{+,m}$ are[7],

$$z_{+,m} = 2m(s + 2z_e) + z_0 \quad for \quad positive \quad sources \tag{3.17}$$

$$z_{+,m} = 2m(s + 2z_e) - 2z_e - z_0 \quad for \quad negative \quad sources \tag{3.18}$$

It is necessary to fulfill the supplementary boundary condition of $\phi = 0$ besides other requirements. This condition can be resolved by incorporating the inclusion of dipoles in close proximity to the plane located at z = 2d. However, the boundary requirement at z=0 is no longer satisfied for t>2d/c. In order to met the boundary conditions at all times, it is necessary to incorporate an endless number of dipole pairs. The quantity of light sources needed in practical applications is contingent upon the optical properties of the plate and the designated time frame for calculating reflectance or transmittance values.

So the expression of the transmission can be written as[7],

$$T(\rho, t) = \frac{exp(-\mu_a vt) - \frac{\rho^2}{4Dvt}}{2(4\pi Dv)^{3/2} t^{5/2}} \sum_{m=-\infty}^{+\infty} [z_{1,m} exp(-\frac{z_{1,m}^2}{4Dvt}) - z_{2,m} exp(-\frac{z_{2,m}^2}{4Dvt})] \tag{3.19}$$

where,

$$z_{1,m} = -2ms - 4mz_e - z_0 \tag{3.20}$$

$$z_{2,m} = -2ms - (4m - 2)z_e + z_0 \tag{3.21}$$

For comparison, the simulation results and the analytical solution are depicted on a single graph, as illustrated in Figure.3.9. The geometry used in this analysis has a thickness of 20 mm and a maximum mesh size of 0.1 mm. The results of curve fitting will be shown in the next section.

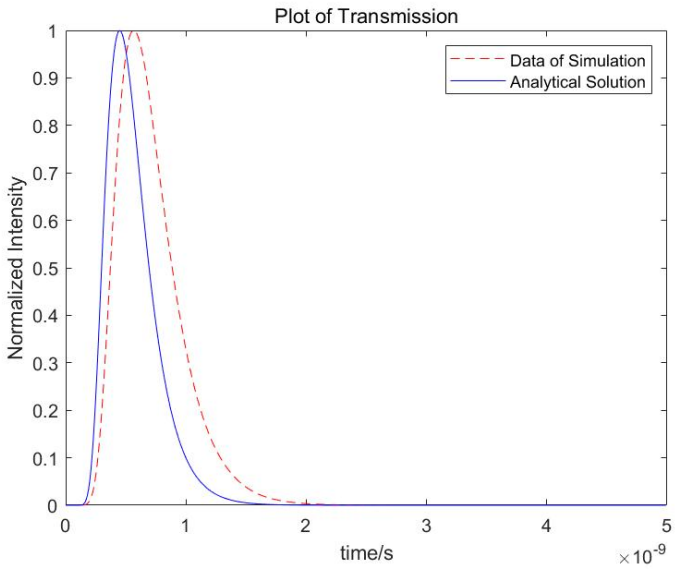

Figure 3.9: Comparison between Simulation Results and Analytical Solution When Source is Collimated Beam

3.5. Results

In this section, the effect of geometry and mesh size on the accuracy of simulation results in this finite element simulation approach will be explored. The smaller the error, the higher the accuracy

Thickness(mm)	$\mu_s^{'}(\times 10^{-3} mm^{-1})$	Error	$\mu_a(\times 10^{-3} mm^{-1})$	Error
20	1810.6	0.03%	23.0887	10%
30	1810.1	0.0055%	22.2849	6%
40	1799.3	0.59%	21.8549	4.1%
50	1821.8	0.65%	21.9571	4.6%

Table 3.1: Isotropic Point Source: Fitting Results and Errors of Coefficients($\mu_s^{'}$ and μ_a) While Changing Thickness

The results of curve fitting and the corresponding errors, which are compared with the reference value, are presented in Table 4.1.

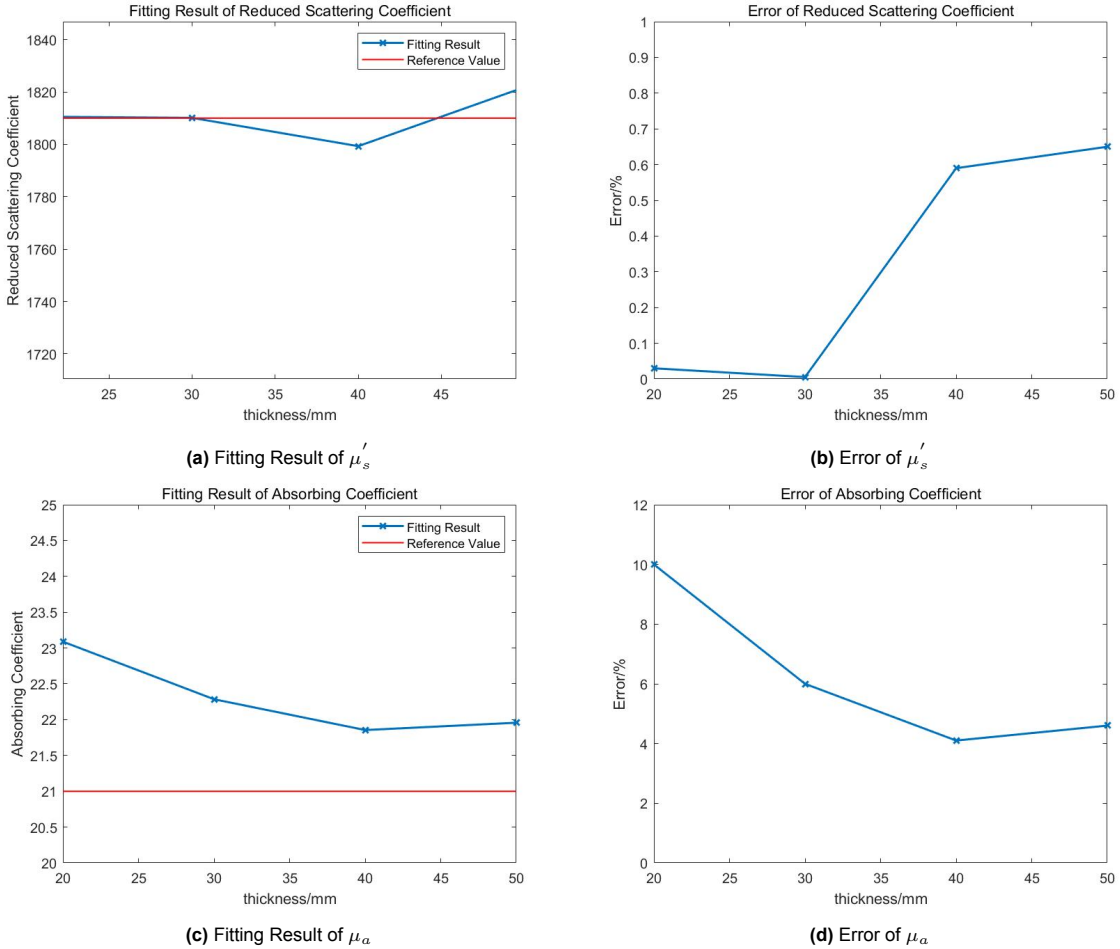

(a) Fitting Result of $\mu_s^{'}$

(b) Error of $\mu_s^{'}$

(c) Fitting Result of μ_a

(d) Error of μ_a

Figure 3.10: Plot of Fitting Results and Errors

Table 3.2 displays the reduced scattering coefficients produced by fitting the simulated data and the error trend between the fitting results and the original values of the reduced scattering coefficients ($\mu_s^{'}$)

.

Thickness(mm)	$\mu_s^{'}(\times 10^{-3} mm^{-1})$	Error	$\mu_a(\times 10^{-3} mm^{-1})$	Error
2	3929.5	117.10%	71.8876	117.10%
5	2373.2	31.12%	3.6688	82.53%
10	2072.3	14.49%	10.3781	50.58%
20	1971.1	8.90%	16.5445	21.22%
30	1930.4	6.65%	18.1461	13.59%
40	1933.2	6.81%	19.3936	7.65%
50	1912.8	5.68%	19.7222	6.08%

Table 3.2: Collimated Beam: Fitting Results and Errors of Coefficients($\mu_s^{'}$ and μ_a While Changing Thickness

The comparison of the fitting results with the original values is represented by a line graph, which is shown in Figure 3.11a. Where the blue line shows the fitted values and the orange line shows the original values. The trend of the error of the simulation results and the analytical solutions is shown in the 3.11c,

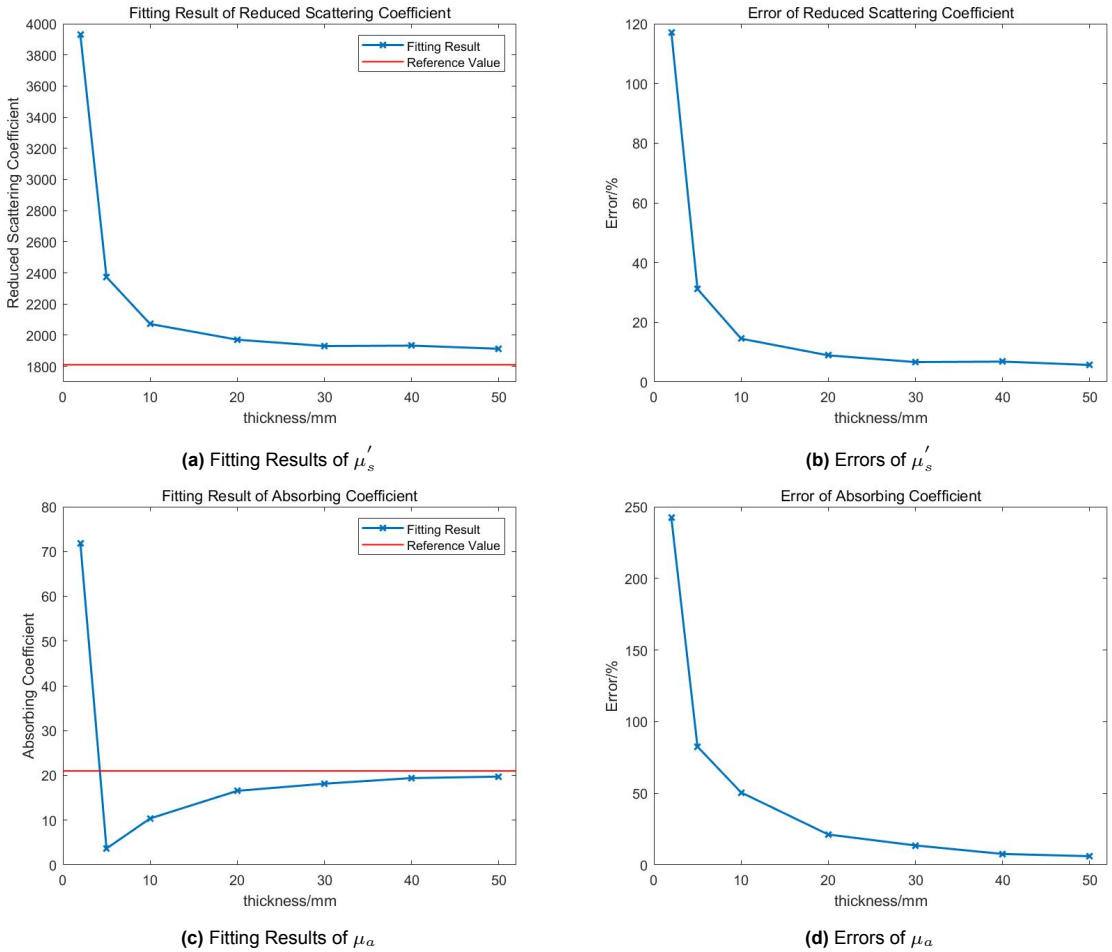

(a) Fitting Results of $\mu_s^{'}$

(b) Errors of $\mu_s^{'}$

(c) Fitting Results of μ_a

(d) Errors of μ_a

Figure 3.11: Plot of Fitting Results and Errors

The comparison of the fitting results to the original values and the trend of the error demonstrates that the simulation's accuracy improves as the geometry develops. When the dimension is very small, which is less than or equal to 10mm, the simulation results is very inaccurate. And at a thickness of 20 mm, the scattering coefficient error is less than 10%, and the absorption coefficient error is less than 10% when the thickness 40 mm.

In the study of the effect of mesh size on the simulation results, the geometry kept constant. Table.3.3 shows the curve fitting results and the error.

Meshpara	$\mu_s^{'}(\times 10^{-3} mm^{-1})$	Error	$\mu_a(\times 10^{-3} mm^{-1})$	Error
1	1970.7	8.88%	16.457	21.63%
2	1954.1	7.96%	16.124	23.22%
3	1940.8	7.23%	15.8204	24.66%
4	1956.4	8.09%	16.2161	22.78%
5	1978.6	9.31%	16.6347	20.79%

Table 3.3: Fitting Results and Errors of Coefficients($\mu_s^{'}$ and μ_a While Changing Mesh Size)

The Figure.3.12 illustrates the outcomes of the fitting process in comparison to the reference values when the mesh size increases, as well as the the observed patterns in the errors.

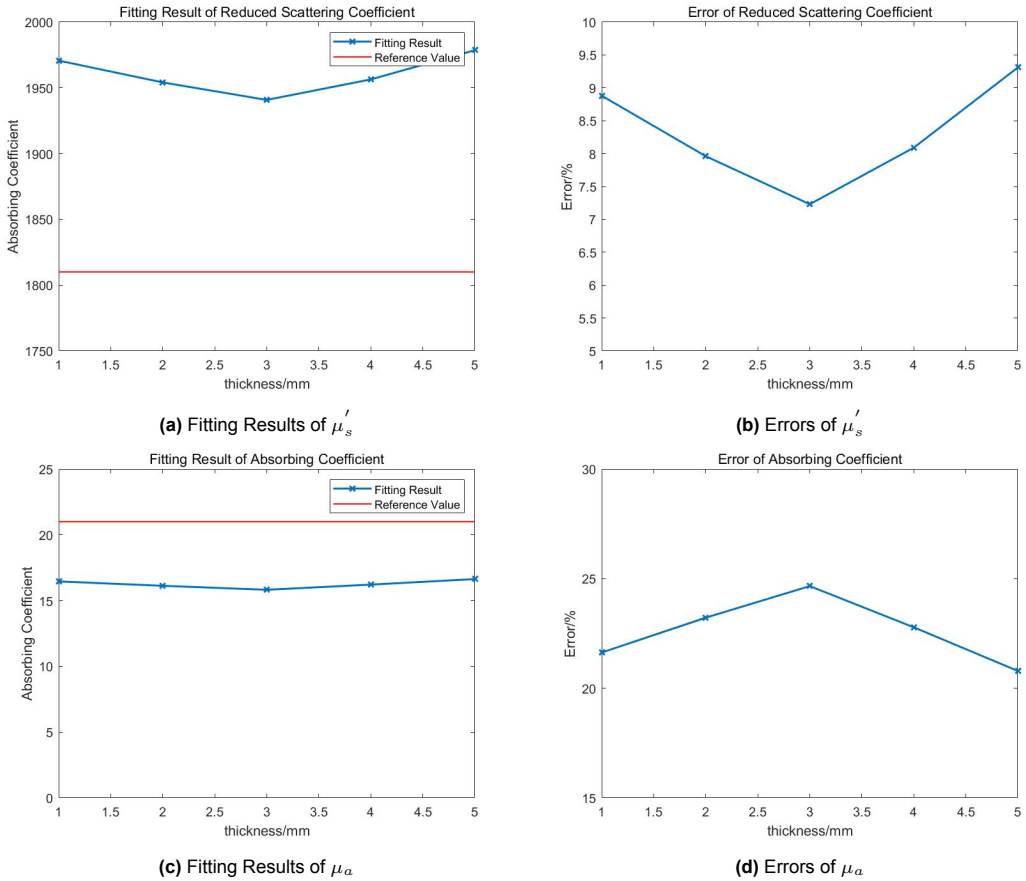

(a) Fitting Results of $\mu_s^{'}$

(b) Errors of $\mu_s^{'}$

(c) Fitting Results of μ_a

(d) Errors of μ_a

Figure 3.12: Plot of Fitting Results and Errors While Changing Mesh Size

When mesh sizes is less than or eual to z_0, the size of the mesh has no significant effect on the simulation results. In addition, the error is essentially consistent with the proportion of the error corresponding to 20 mm in the dimension analysis in the preceding section.

3.6. Summary

This chapter examines the simulation of the diffusion equation of Radiative Transfer Equation (RTE) using the Coefficient Form PDE in the COMSOL Multiphysics 5.6. The diffusion coefficients and absorption coefficients of the tissues are determined by fitting the simulation results using the least squares method through the **lsqcurvefit** function in MATLAB. These coefficients are then compared with the reference values. This study investigates the influence of geometry and mesh size on the results of simulations while using the Finite Element Method for simulating the diffusion equation. Various temporal resolutions and fitting functions were also tested ane selected and chosen during the experiment.

The results indicate that when exposed to collimated light, there is an inverse relationship between the geometric size and the discrepancy between the simulation results and the reference value. Consequently, larger geometric sizes yield more precise simulation results. Conversely, when subjected to an isotropic point light source, no discernible trend emerges between the geometric size and the accuracy of the simulation. Thus, the impact can be deemed negligible. When the mesh size is smaller than or equal to z_0, there is no discernible correlation between the simulation accuracy and the mesh size. Additionally, the simulation accuracy remains unaffected by changes in the mesh size.

4

Case Study: Simulation of CTE

In this chapter, the simulation of the correlation transfer equation (CTE) diffusion equation in COMSOL Multiphysics 5.6 using Coefficient Form PDE is performed, similar to the previous chapter's simulation of the RTE. The simulation results are subjected to fitting utilizing the least squares method by using the **lsqcurvefit** function in MATLAB. Subsequently, the value of BFi is ascertained and compared to the reference value. This study examines the impact of geometry and mesh size on the outcomes of simulating the correlation transfer equation (CTE) within the finite element method framework.

4.1. Simulation

The correlation transport equation can be simplified to the correlation diffusion equation when considering the correlation fluence rate (G_1), the diffusion equation simulated in this section is,

$$[\nabla \cdot (D(\mathbf{r})\nabla) - \mu_a(\mathbf{r}) - \frac{\alpha}{3}\mu_s^{'}k_0^2\langle\Delta r^2(\tau)\rangle]G_1(\mathbf{r},\tau) = -S(\mathbf{r}) \tag{4.1}$$

As mentioned earlier, the Brownian diffusion coefficient, denoted as D_B, characterizes the diffusion of particles in a medium. The parameter α quantifies the fraction of photon scattering events that arise from the motion of particles inside the medium. In the field of biological tissue research, αD_B is commonly referred to as the blood flow index(BFi)[34], serving as a quantitative indicator of tissue perfusion. In prior research, the typical range for the value of DB or αDB has been observed to be between $(1 \sim 3) \times 10^{-8} cm^2/s$[3][13]. Therefore, in this report, a value of $\alpha D_B = 2.5 \times 10^{-8} cm^2/s$ was selected.

The wavelength range of visible light is from 400 to 780 nm, and k_0 represents the wave number of light within a certain medium, which is,

$$k_0 = \frac{2\pi}{\lambda} \tag{4.2}$$

According to the previous chapters, we have,

$$D = \frac{1}{3\mu_s^{'}} \tag{4.3}$$

In the simulation of the CTE, fixed values of $\mu_a = 0.021mm^{-1}$ and $\mu_s^{'} = 1.81mm^{-1}$, which are the same with the simulation of RTE, were selected for the absorption coefficient μ_a and reduced scattering coefficients $\mu_s^{'}$, respectively.

$$\langle \Delta r^2(\tau) \rangle = 6D_B\tau \tag{4.4}$$

Just as the simulation of RTE requires the consideration of boundary conditions, the simulation of CTE also necessitates the inclusion of boundary conditions. In the simulation of CTE, the partial-flux boundary condition is,

$$G_1(\mathbf{r}, \tau) = z_b\hat{n} \cdot \nabla G_1(\mathbf{r}, \tau) \tag{4.5}$$

And the extrapolated zero boundary condition is,

$$G_1(z = z_b) = 0 \tag{4.6}$$

For this simulation, The investigation of the impact of geometry size on simulation outcomes in the context of CTE should involve maintaining constant values for all other parameters while solely manipulating the size variable, which is the same with simulating RTE. For the simulation. Figure.4.1 shows the simulation result when the thicknesses of the geometry vary.

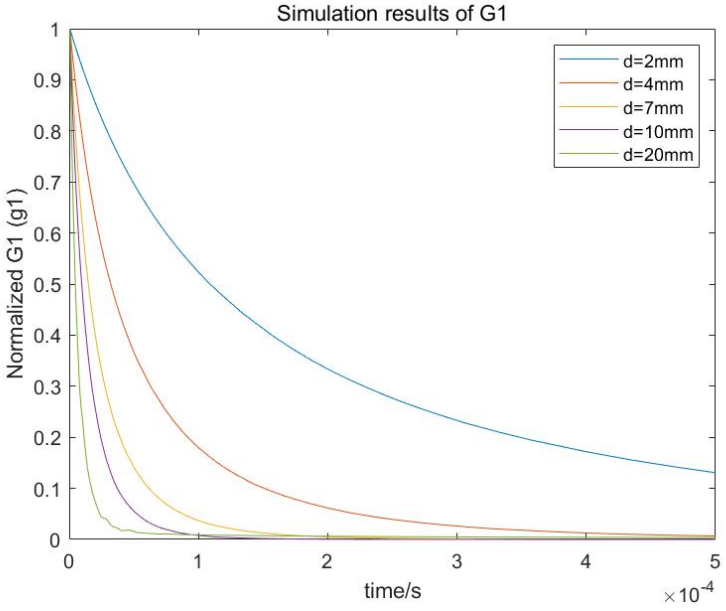

Figure 4.1: Simulation Results While Changing Thickness

The configuration while investigating the impact of mesh size is the same as that in RTE, shown in the Figure.4.5. Figure.4.2a depicts the entirety of the plot while Figure.4.2b provides a more detailed representation of the plot.

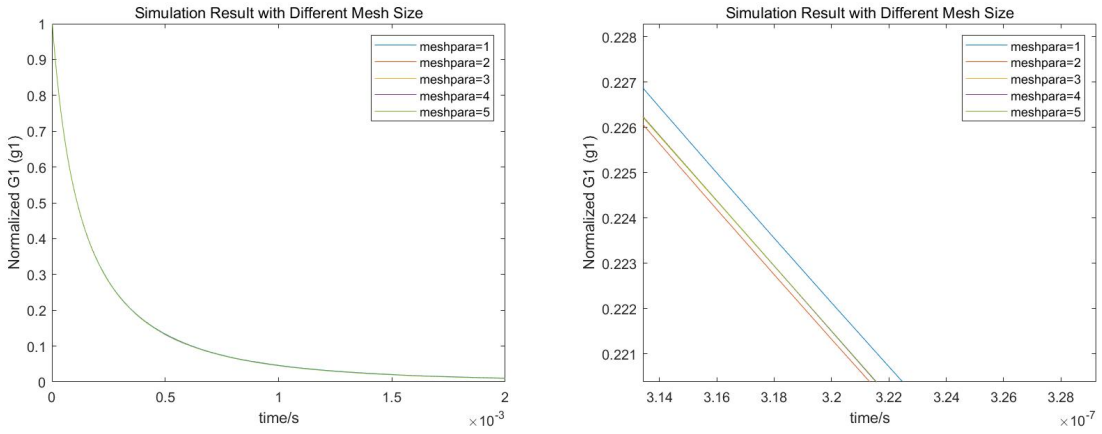

(a) Simulation Results **(b)** Detailed plot

Figure 4.2: Simulation Results While Changing Mesh Size

4.2. Curve fitting

In the frequency domain, the homogeneous semi infinite Green's function is,

$$G_0(\rho, z) = \frac{v}{4\pi}[\frac{exp(-kr_1)}{r_1} - \frac{exp(-kr_b}{r_b}] \tag{4.7}$$

where,

$$\begin{cases} r_1 = \sqrt{(z - z_0)^2 + \rho^2}, \\ r_b = \sqrt{(z + 2z_b + z_0)^2 + \rho^2}. \end{cases} \tag{4.8}$$

The correlation fluence rate $G_1(\mathbf{r}, \tau)$ is,

$$G_1(\mathbf{r}, \tau) = \int_{4\pi} G_1^T(\mathbf{r}, \hat{s}, \tau) ds = \langle \mathbf{E}^*(\mathbf{r}, t) \cdot \mathbf{E}(\mathbf{r}, t) \rangle \tag{4.9}$$

And the solution of the equation of the equation 4.1 in semi-infinite medium is,

$$G_1(\rho, z, \tau) = \frac{v}{4\pi D}[\frac{exp(-K(\tau)r_1)}{r_1} - \frac{exp(-K(\tau)r_b}{r_b}] \tag{4.10}$$

where,

$$K(\tau) = \sqrt{(\mu_a + \alpha\mu_s' k_0^2 \langle \Delta r^2(\tau) \rangle / 3)/D} \tag{4.11}$$

Then, the expression of $K(\tau)$ can be simplified as,

$$K(\tau) = \sqrt{3\mu_a \mu_s'^2 + 6\alpha D_B \mu_s'^2 k_0^2 \tau} \tag{4.12}$$

The images of the simulation results and the analytical solution are plotted on a single graph, employing a configuration with d = 2 mm and the maximum size of the mesh is 0.1 mm as an example, as shown in Figure.4.3.

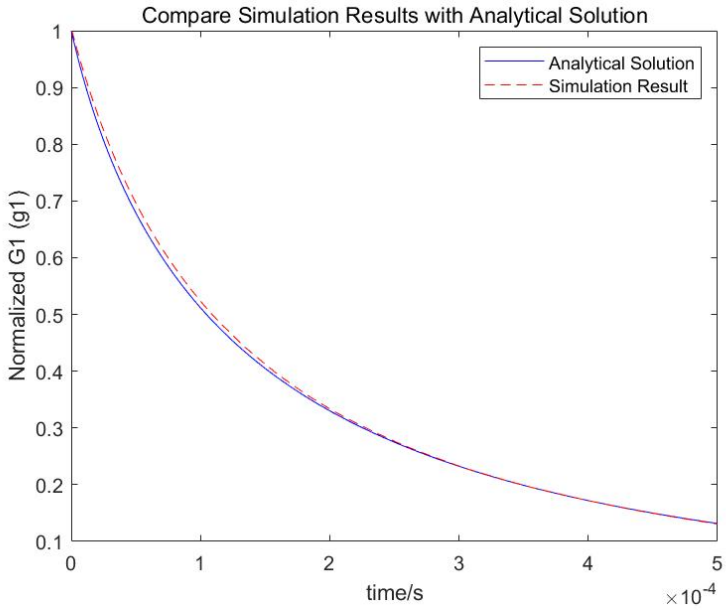

Figure 4.3: Comparison of Simulation Result and Analytical Solution

4.3. result

Table 4.1 displays the BFi(αD_B) produced by fitting the simulated data and the error trend between the fitting results and the original values of the reduced scattering coefficients ($\mu_s^{'}$) when the dimension is increasing.

Thickness(mm)	$\alpha D_B(\times 10^{-8} cm^2/s)$	Error
2	2.486	0.56%
4	2.6032	4.13%
7	2.6423	5.69%
10	2.6334	5.34%
20	2.3984	4.06%

Table 4.1: Curve Fitting Results of αD_B While Changing Thickness

The comparison of the fitting results with the original values is represented by a line graph, which is shown in Figure 4.4a. Where the blue line shows the fitted values and the orange line shows the original values. The trend of the error of the simulation results and the analytical solutions is shown in the 4.4b,

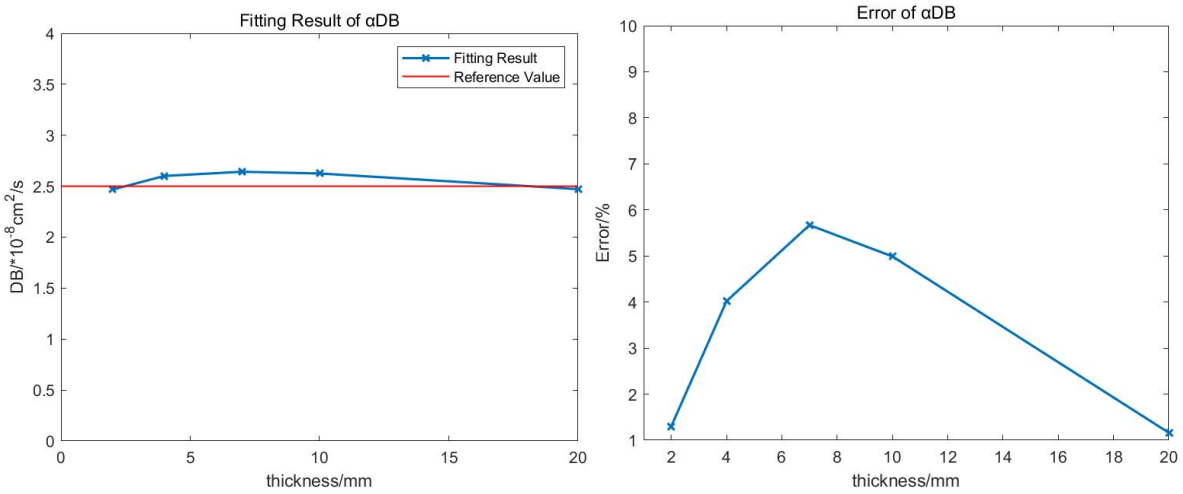

(a) Fitting Results **(b)** Errors

Figure 4.4: Plot of Fitting Results and Errors While Changing Thickness

As the dimensionality increases, the gap between the fitted values and the reference values exhibits a fluctuating pattern, characterized by an initial increase followed by a subsequent drop. However, it is noteworthy that the overall error consistently remains below 10 percent. There appears to be no discernible pattern indicating a consistent increase or decrease in simulation accuracy as the dimension within the specified size range increases.

The fitting results are presented in Table.4.2, where the geometry remains constant while the mesh size is varied. Additionally, the error values are displayed, indicating the extent to which they depart from the initial values.

meshpara	$\alpha D_B(\times 10^{-8} cm^2/s)$	Error
1	2.4837	0.652%
2	2.4861	0.556%
3	2.486	0.560%
4	2.4861	0.556%
5	2.486	0.560%

Table 4.2: Curve Fitting Results of αD_B While Changing Mesh Size

The results of the fitting procedure are depicted in Figure 4.5, which showcases the comparison between the fitted values and the reference values when the mesh size is decreased, as well as the discernible patterns identified in the errors.

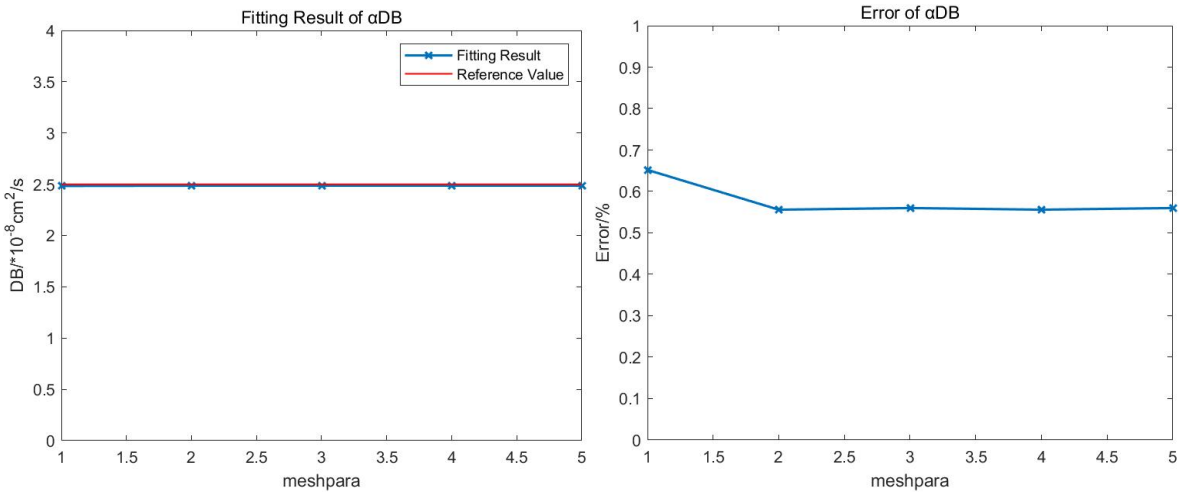

(a) Fitting Results **(b)** Errors

Figure 4.5: Plot of Fitting Results and Errors While Changing Mesh Size

The observed data does not exhibit any identifiable trend about the influence of mesh sizes within the specified ranges on the precision of the simulations.

4.4. Summary

This chapter focuses on the simulation of the diffusion equation of the correlation transfer equation (CTE) in COMSOL Multiphysics 5.6. The simulation is conducted by Coefficient Form PDE, which is the same approach as simulating the radiative transfer equation (RTE). The simulation results are analyzed using the least squares method through the utilization of the **lsqcurvefit** function in MATLAB. This approach is employed to ascertain the value of BFi and subsequently compare it with the reference value. The objective is to examine the impact of geometry and mesh size on the outcomes obtained from simulating the correlation transfer equation (CTE) within the finite element method.

The findings indicate that the discrepancy between the estimated and actual values varies but remains below 10% in aggregate as the dimensions increase. Additionally, when the mesh size is equal to or smaller than z_0, the discrepancy remains relatively constant as the mesh becomes more refined. There appears to be no discernible pattern regarding the impact of dimensions and mesh sizes within the discussed ranges on the accuracy of the simulations.

5

Results and Discussion

5.1. Results

Based on the findings presented in Chapters 3 and 4, as well as the subsequent examination of these findings, it is possible to draw straightforward conclusions. In the context of finite element simulations, it has been observed that the accuracy of simulation results for the radiative transfer equation (RTE) improves with larger geometric dimensions. Specifically, thicker tissues yield more reliable results. Conversely, variations in mesh size do not exert a substantial influence on the simulation outcomes. On the other hand, when simulating the correlation transfer equation (CTE), neither the mesh size nor the geometric dimensions exhibit a significant impact on the simulation results.

5.2. Discussion

There are multiple potential explanations for the presence of the error. Firstly, the complexity of the boundary conditions for solving the RTEand the CTE using the diffusion equation may contribute to this error. This complexity is particularly evident in the wireless board model, where the Partial Differential Equation (PDE) in coefficient form acts as a generic interface and is unable to simultaneously satisfy all the boundary conditions. Secondly, the limitations inherent in modeling with the diffusion approximation could also be a factor. Additionally, the width of the model and potential computational errors in the fit function may have an impact on the results. These are just a few examples of the various factors that could contribute to the observed error.

The aforementioned conclusions were derived by comparing the results of mathematical fitting of simulation data with reference values. This involved calculating the errors and analyzing the patterns of error changes. These conclusions were obtained within the specific settings of RTE and CTE. Upon comparing the two entities, it is possible to derive the following conclusions:

- The radiative transport equation (RTE) is simulated using a short-pulse laser source, while the continuous-wave light source is employed in the CTE model.

- When the dimensions are significantly reduced, the simulation outcomes of the Correlation transfer equation (CTE) exhibit a high level of accuracy, whereas the results obtained from the radiative transport equation (RTE) are notably imprecise□which is due to the conditions of solving RTE using the diffusion approximation.

- The simulated radiative transport equation (RTE) has a temporal resolution of 0.1 nanoseconds and encompasses a research range spanning from 0 to 5 nanoseconds. In contrast, the simulated Correlation transfer equation (CTE) possesses a time resolution of 0.5 microseconds and encompasses a study range spanning from 0 to 500 microseconds. If the Correlation Transfer Equation (CTE) is modified to decrease the temporal resolution and study range, the resulting image will exhibit an approximate linear relationship, as depicted in Figure 1.

Outlook

Hence, in the event that additional investigation is sought, such as integrating or establishing correlations between the two models to derive deeper insights, it is imperative to conduct further debugging of the model in accordance with established principles, thereby enhancing its broader applicability.

6

Conclusion

The present report commences with a concise introduction to the theory of diffuse optics and the modeling of light propagation. In the next section, we show a finite element simulation of the diffusion equation using COMSOL. This simulation serves as a model for the radiative transport equation and the correlation transport equation, under the assumption that the conditions necessary for approximating the transport equation using diffusion theory are satisfied. The simulation of light propagation and correlation inside diffusion tissue involves the solution of the diffusion equation. The quantification and summarization of the model's accuracy variability in relation to geometry and mesh size is achieved by manipulating the parameters of the model. In conclusion, this study presents a summary and proposal of potential directions for further research.

References

[1] Beer. “Bestimmung der Absorption des rothen Lichts in farbigen Flüssigkeiten”. In: *Annalen der Physik* 162.5 (1852), pp. 78–88. DOI: https://doi.org/10.1002/andp.18521620505. eprint: https://onlinelibrary.wiley.com/doi/pdf/10.1002/andp.18521620505. URL: https://onlinelibrary.wiley.com/doi/abs/10.1002/andp.18521620505.

[2] T Binzoni et al. “The use of the Henyey–Greenstein phase function in Monte Carlo simulations in biomedical optics”. In: *Physics in Medicine & Biology* 51.17 (Aug. 2006), N313. DOI: 10.1088/0031-9155/51/17/N04. URL: https://dx.doi.org/10.1088/0031-9155/51/17/N04.

[3] David A Boas, LE Campbell, and Arjun G Yodh. “Scattering and imaging with diffusing temporal field correlations”. In: *Physical review letters* 75.9 (1995), p. 1855.

[4] R. Bonner and R. Nossal. “Model for laser Doppler measurements of blood flow in tissue”. In: *Appl. Opt.* 20.12 (June 1981), pp. 2097–2107. DOI: 10.1364/AO.20.002097. URL: https://opg.optica.org/ao/abstract.cfm?URI=ao-20-12-2097.

[5] J David Briers. “Laser Doppler, speckle and related techniques for blood perfusion mapping and imaging”. In: *Physiological Measurement* 22.4 (Oct. 2001), R35. DOI: 10.1088/0967-3334/22/4/201. URL: https://dx.doi.org/10.1088/0967-3334/22/4/201.

[6] Benjamin Chu. In: (1991). DOI: https://doi.org/10.1016/B978-0-12-174551-6.X5001-0.

[7] Daniele Contini, Fabrizio Martelli, and Giovanni Zaccanti. “Photon migration through a turbid slab described by a model based on diffusion approximation. I. Theory”. In: *Applied optics* 36.19 (1997), pp. 4587–4599.

[8] Milena Corredig and Marcela Alexander. “Food emulsions studied by DWS: recent advances”. In: *Trends in Food Science & Technology* 19.2 (2008), pp. 67–75. ISSN: 0924-2244. DOI: https://doi.org/10.1016/j.tifs.2007.07.014. URL: https://www.sciencedirect.com/science/article/pii/S0924224407002324.

[9] Mitchell A. Davis, S. M. Shams Kazmi, and Andrew K. Dunn. “Imaging depth and multiple scattering in laser speckle contrast imaging”. In: *Journal of Biomedical Optics* 19.8 (2014), p. 086001. DOI: 10.1117/1.JBO.19.8.086001. URL: https://doi.org/10.1117/1.JBO.19.8.086001.

[10] Hamid Dehghani et al. “Near infrared optical tomography using NIRFAST: Algorithm for numerical model and image reconstruction”. In: *Communications in numerical methods in engineering* 25.6 (2009), pp. 711–732.

[11] D T Delpy et al. “Estimation of optical pathlength through tissue from direct time of flight measurement”. In: *Physics in Medicine & Biology* 33.12 (Dec. 1988), p. 1433. DOI: 10.1088/0031-9155/33/12/008. URL: https://dx.doi.org/10.1088/0031-9155/33/12/008.

[12] André Y. Denault et al. “Chapter 7 - Near-Infrared Spectroscopy”. In: (2018). Ed. by Hemanshu Prabhakar, pp. 179–233. DOI: https://doi.org/10.1016/B978-0-12-809915-5.00007-3. URL: https://www.sciencedirect.com/science/article/pii/B9780128099155000073.

[13] T Durduran et al. “Diffuse optics for tissue monitoring and tomography”. In: *Reports on Progress in Physics* 73.7 (June 2010), p. 076701. DOI: 10.1088/0034-4885/73/7/076701. URL: https://dx.doi.org/10.1088/0034-4885/73/7/076701.

[14] Lord Rayleigh F.R.S. “XXXIV. On the transmission of light through an atmosphere containing small particles in suspension, and on the origin of the blue of the sky”. In: *The London, Edinburgh, and Dublin Philosophical Magazine and Journal of Science* 47.287 (1899), pp. 375–384. DOI: 10.1080/14786449908621276.

[15] Thomas J Farrell, Michael S Patterson, and Brian Wilson. “A diffusion theory model of spatially resolved, steady-state diffuse reflectance for the noninvasive determination of tissue optical properties in vivo”. In: *Medical physics* 19.4 (1992), pp. 879–888.

[16] Grant R. Fowles. “Introduction to modern optics”. In: 1968.

[17] J.L. Harden and V. Viasnoff. “Recent advances in DWS-based micro-rheology”. In: *Current Opinion in Colloid & Interface Science* 6.5 (2001), pp. 438–445. ISSN: 1359-0294. DOI: https://doi.org/10.1016/S1359-0294(01)00115-7. URL: https://www.sciencedirect.com/science/article/pii/S1359029401001157.

[18] In: *Symmetry and Spectroscopy*. Ed. by Harris and Bertolucci. Dover Publications, 1989. ISBN: 978-0-486-66144-5.

[19] Erhunmwun. ID and Ikponmwosa. UB. “Review on finite element method”. In: *Journal of Applied Sciences and Environmental Management* 21.5 (2017), pp. 999–1002.

[20] Frans F. Jöbsis. “Noninvasive, Infrared Monitoring of Cerebral and Myocardial Oxygen Sufficiency and Circulatory Parameters”. In: *Science* 198.4323 (1977), pp. 1264–1267.

[21] SAM Kirmani et al. “Simulation of Diffuse Optical Tomography using COMSOL Multiphysics®”. In: *Excerpt from the Proceedings of the 2016 COMSOL. Boston* (2016).

[22] “1 - Essentials of the COVID-19 coronavirus”. In: *Data Science for COVID-19*. Ed. by Utku Kose et al. Academic Press, 2022, pp. 1–25. ISBN: 978-0-323-90769-9. DOI: https://doi.org/10.1016/B978-0-323-90769-9.00020-7.

[23] Dominik Marti et al. “MCmatlab: an open-source, user-friendly, MATLAB-integrated three-dimensional Monte Carlo light transport solver with heat diffusion and tissue damage”. In: *Journal of Biomedical Optics* 23.12 (2018), p. 121622. DOI: 10.1117/1.JBO.23.12.121622. URL: https://doi.org/10.1117/1.JBO.23.12.121622.

[24] Mansfield Merriman. *A List of Writings Relating to the Method of Least Squares: With Historical and Critical Notes*. Vol. 4. Academy, 1877.

[25] *Monte Carlo modeling of light propagation in highly scattering tissues. I. Model predictions and comparison with diffusion theory | IEEE Journals & Magazine | IEEE Xplore*. URL: https://ieeexplore.ieee.org/abstract/document/1173624?casa_token=q_p8a5Rpvs4AAAAA:O8HkyrxdUUJwiIvR-i131Ac2ltElHmkwwbmgMtZIq8Ph_kogLfnO-zTfarijv9bAHJ2jhw-GjA (visited on 07/12/2023).

[26] Markus Ninck, Markus Untenberger, and Thomas Gisler. “Diffusing-wave spectroscopy with dynamic contrast variation: disentangling the effects of blood flow and extravascular tissue shearing on signals from deep tissue”. In: *Biomed. Opt. Express* 1.5 (Dec. 2010), pp. 1502–1513. DOI: 10.1364/BOE.1.001502. URL: https://opg.optica.org/boe/abstract.cfm?URI=boe-1-5-1502.

[27] Juliette J. Selb et al. “Improved sensitivity to cerebral hemodynamics during brain activation with a time-gated optical system: analytical model and experimental validation”. In: *Journal of Biomedical Optics* 10.1 (2005), p. 011013. DOI: 10.1117/1.1852553. URL: https://doi.org/10.1117/1.1852553.

[28] Zhenqi Shi and Carl A. Anderson. “Pharmaceutical Applications of Separation of Absorption and Scattering in Near-Infrared Spectroscopy (NIRS)”. In: *Journal of Pharmaceutical Sciences* 99.12 (2010), pp. 4766–4783. ISSN: 0022-3549. DOI: https://doi.org/10.1002/jps.22228. URL: https://www.sciencedirect.com/science/article/pii/S0022354915323893.

[29] Xianlin Song et al. “Simulation study of interaction of pulse laser with brain using finite element analysis”. In: *Biophotonics and Biomedical Microscopy*. Ed. by Sumeet Mahajan and Amanda J. Wright. Online Only, United Kingdom: SPIE, Oct. 2020, p. 13. ISBN: 978-1-5106-3970-6 978-1-5106-3971-3. DOI: 10.1117/12.2582931. URL: https://www.spiedigitallibrary.org/conference-proceedings-of-spie/11575/2582931/Simulation-study-of-interaction-of-pulse-laser-with-brain-using/10.1117/12.2582931.full (visited on 07/06/2023).

[30] “Source of error in calculation of optical diffuse reflectance from turbid media using diffusion theory”. In: *Computer Methods and Programs in Biomedicine* 61.3 (2000), pp. 163–170. ISSN: 0169-2607. DOI: https://doi.org/10.1016/S0169-2607(99)00041-3.

[31] Jason Sutin et al. “Time-domain diffuse correlation spectroscopy”. In: *Optica* 3.9 (Sept. 2016), pp. 1006–1013. DOI: 10.1364/OPTICA.3.001006. URL: https://opg.optica.org/optica/abstract.cfm?URI=optica-3-9-1006.

[32] Ao Teng et al. “Simulation study of interaction of pulse laser with brain using COMSOL”. In: *SPIE Future Sensing Technologies*. Ed. by Masafumi Kimata, Joseph A. Shaw, and Christopher R. Valenta. Vol. 11525. International Society for Optics and Photonics. SPIE, 2020, 115252J. DOI: 10.1117/12.2584025. URL: https://doi.org/10.1117/12.2584025.

[33] Nathan Tomer, Andrew McGlone, and Rainer Künnemeyer. “Validated multi-wavelength simulations of light transport in healthy onion”. In: *Computers and Electronics in Agriculture* 146 (2018), pp. 22–30.

[34] Danil Tyulmankov. “Time-domain diffuse correlation spectroscopy: instrument prototype, preliminary measurements, and theoretical modeling”. PhD thesis. Massachusetts Institute of Technology, 2017.

[35] Vasudevan. Vysakh and Sujatha. N. “Immediate subsurface skin blood flow monitoring using diffuse correlation spectroscopy: finite element simulations”. In: *Tissue Optics and Photonics II*. Vol. 12147. SPIE. 2022, pp. 52–56.

[36] Lihong Wang, Steven L. Jacques, and Liqiong Zheng. “MCML—Monte Carlo modeling of light transport in multi-layered tissues”. In: *Computer Methods and Programs in Biomedicine* 47.2 (1995), pp. 131–146. ISSN: 0169-2607. DOI: https://doi.org/10.1016/0169-2607(95)01640-F. URL: https://www.sciencedirect.com/science/article/pii/016926079501640F.

[37] Lihong V. Wang. “Rapid modeling of diffuse reflectance of light in turbid slabs”. In: *J. Opt. Soc. Am. A* 15.4 (Apr. 1998), pp. 936–944. DOI: 10.1364/JOSAA.15.000936. URL: https://opg.optica.org/josaa/abstract.cfm?URI=josaa-15-4-936.

[38] In: *Biomedical Optics*. Ed. by LV Wang & HI Wu. Wiley, 2007. ISBN: 978-0-471-74304-0.

[39] K. M. Yoo, Feng Liu, and R. R. Alfano. “When does the diffusion approximation fail to describe photon transport in random media?” In: *Phys. Rev. Lett.* 64 (22 May 1990), pp. 2647–2650. DOI: 10.1103/PhysRevLett.64.2647. URL: https://link.aps.org/doi/10.1103/PhysRevLett.64.2647.

[40] Caigang Zhu and Quan Liu. “Review of Monte Carlo modeling of light transport in tissues”. In: *Journal of Biomedical Optics* 18.5 (2013), p. 050902. DOI: 10.1117/1.JBO.18.5.050902. URL: https://doi.org/10.1117/1.JBO.18.5.050902.